25. Calfon M, Zeng H, Urano F, Till JH, Hubbard SR, Harding HP, Clark SG, Ron D. IRE1 couples endoplasmic reticulum load to secretory capacity by processing the XBP-1 mRNA. *Nature* 2002;**415**:92–6
26. Shen X, Ellis RE, Lee K, Liu CY, Yang K, Solomon A, Yoshida H, Morimoto R, Kurnit DM, Mori K, Kaufman RJ. Complementary signaling pathways regulate the unfolded protein response and are required for C. elegans development. *Cell* 2002;**107**:893–903
27. Yoshida H, Matsui T, Yamamoto A, Okada T, Mori K. XBP1 mRNA is induced by ATF6 and spliced by IRE1 in response to ER stress to produce a highly active transcription factor. *Cell* 2002;**107**:881–891
28. Lozon TI, Eastman AJ, Matute-Bello G, Chen P, Hallstrand TS, Altemeier WA. PKR-dependent CHOP induction limits hyperoxia-induced lung injury. *Am J Physiol Lung Cell Mol Physiol* 2011;**300**:L422–9
29. Southwood CM, Garbern J, Jiang W, Gow A. The unfolded protein response modulates disease severity in Pelizaeus-Merzbacher disease. *Neuron* 2002;**36**:585–96
30. Adelusi SA, Salako LA. Tissue and blood nconcentration of chloroquine following chronic administration in the rats. *J Pharm Pharmacol* 1982;**34**:733–5
31. Ozcan U, Yilmaz E, Ozcan L, Furuhashi M, Vaillancourt E, Smith RO, Görgün CZ, Hotamisligil GS. Chemical chaperones reduce ER stress and restore glucose homeostasis in a mouse model of type 2 diabetes. *Science* 2006;**313**:1137–40
32. Egan ME, Pearson M, Weiner SA, Rajendran V, Rubin D, Glöckner-Pagel J, Canny S, Du K. Lukacs GL, Caplan MJ. Curcumin, a major constituent of turmeric, corrects cystic fibrosis defects. *Science* 2004;**304**:600–2
33. Yu L-H, Morimura T, Numata Y, Inoue N, Antalfy B, Goto YI, Deguchi K, Osaka H, Inoue K. Effect of curcumin in a mouse model of Pelizaeus-Merzbacher disease. *Mol Genet Metab* 2012;**106**:108–14
34. Kim I, Xu W, Reed JC. Cell death and endoplasmic reticulum stress: diseasse relevance and therapeutic opportunities. *Nat Rev Drug Genet* 2008;**7**:1013–30
35. Slater AF, Cerami A. Inhibition by chloroquine of a novel haem polymerase enzyme activity in malaria trophozoites. *Nature* 1992;**355**:167–9
36. Lee SJ, Silverman E, Bargman JM. The role of antimalarial agents in the treatment of SLE and lupus nephritis. *Nat ReV Nephrol* 2011;**7**:718–29
37. Boyce M, Bryant KF, Jouss C, Long K. Harding HP, Scheuner D, Kaufman RJ, Ma D, Coen DM, Ron D, Yuan J. A selective inhibitor of eIF2alpha dephosphorylation protects cells from ER stress. *Science* 2005;**307**:935–9
38. Yamamoto K, Tashiro E, Imoto M. Quinotrierixin inhibited ER stress-induced XBP1 mRNA splicing through inhibition of protein synthesis. *Biosci Biotechnol Biochem* 2011;**75**:284–8
39. Saxena S, Cabuy E, Caroni P. A role for motoneuron subtype-selective ER stress in disease manifestations of FALS mice. *Nat Neurosci* 2009;**12**:627–36
40. Han J, Back SH, Hur J, Lin YH, Gildersleeve R, Shan J, Yuan CL, Krokowski D, Wang S, Hatzoglou M, Kilberg MS, Sartor MA, Kaufman RJ. ER-stress-induced transcriptional regulation increases protein synthesis leading to cell death. *Nat Cell Biol* 2013;**15**:481–90
41. Gow A, Wrabet L. CHOP and the endoplasmic reticulum stress response in myelinating glia. *Curr Opin Neurobiol* 2009;**19**:505–10

(Received July 4, 2013, Accepted November 26, 2013)

Please cite this article in press as: Numasawa-Kuroiwa et al., Involvement of ER Stress in Dysmyelination of Pelizaeus-Merzbacher Disease with *PLP1* Missense Mutations Shown by iPSC-..., Stem Cell Reports (2014), http://dx.doi.org/10.1016/j.stemcr.2014.03.007

Stem Cell Reports

Article

ISSCR

OPEN ACCESS

Involvement of ER Stress in Dysmyelination of Pelizaeus-Merzbacher Disease with *PLP1* Missense Mutations Shown by iPSC-Derived Oligodendrocytes

Yuko Numasawa-Kuroiwa,[1,2] Yohei Okada,[1,3,*] Shinsuke Shibata,[1] Noriyuki Kishi,[1] Wado Akamatsu,[1] Masanobu Shoji,[4] Atsushi Nakanishi,[4] Manabu Oyama,[5] Hitoshi Osaka,[6] Ken Inoue,[7] Kazutoshi Takahashi,[8] Shinya Yamanaka,[8] Kenjiro Kosaki,[9] Takao Takahashi,[2] and Hideyuki Okano[1,*]

[1]Department of Physiology, School of Medicine, Keio University, 35 Shinanomachi, Shinjuku-ku, Tokyo 160-8582, Japan
[2]Department of Pediatrics, School of Medicine, Keio University, 35 Shinanomachi, Shinjuku-ku, Tokyo 160-8582, Japan
[3]Department of Neurology, School of Medicine, Aichi Medical University, 1-1 Yazako Karimata, Nagakute, Aichi 480-1195, Japan
[4]Advanced Science Research Laboratories, Takeda Pharmaceutical Company Limited, 26-1 Muraoka-Higashi 2-Chome, Fujisawa, Kanagawa 251-8555, Japan
[5]Department of Dermatology, School of Medicine, Keio University, 35 Shinanomachi, Shinjuku-ku, Tokyo 160-8582, Japan
[6]Department of Pediatrics, Jichi Medical School, 3311-1 Yakushiji, Shimotsuke-shi, Tochigi 329-0498, Japan
[7]Department of Mental Retardation and Birth Defect Research, National Institute of Neuroscience, National Center of Neurology and Psychiatry, 4-1-1 Ogawahigashi-machi, Kodaira-shi, Tokyo 187-8551, Japan
[8]Center for Induced Pluripotent Stem Cell Research and Application, Graduate School of Medicine, Institute for Frontier Medical Sciences, Kyoto University, Kyoto 606-8507, Japan
[9]Center for Medical Genetics, School of Medicine, Keio University, 35 Shinanomachi, Shinjuku-ku, Tokyo 160-8582, Japan
*Correspondence: yohei@a6.keio.jp (Y.O.), hidokano@a2.keio.jp (H.O.)
http://dx.doi.org/10.1016/j.stemcr.2014.03.007

SUMMARY

Pelizaeus-Merzbacher disease (PMD) is a form of X-linked leukodystrophy caused by mutations in the *proteolipid protein 1* (*PLP1*) gene. Although PLP1 proteins with missense mutations have been shown to accumulate in the rough endoplasmic reticulum (ER) in disease model animals and cell lines transfected with mutant *PLP1* genes, the exact pathogenetic mechanism of PMD has not previously been clarified. In this study, we established induced pluripotent stem cells (iPSCs) from two PMD patients carrying missense mutations and differentiated them into oligodendrocytes in vitro. In the PMD iPSC-derived oligodendrocytes, mislocalization of mutant PLP1 proteins to the ER and an association between increased susceptibility to ER stress and increased numbers of apoptotic oligodendrocytes were observed. Moreover, electron microscopic analysis demonstrated drastically reduced myelin formation accompanied by abnormal ER morphology. Thus, this study demonstrates the involvement of ER stress in pathogenic dysmyelination in the oligodendrocytes of PMD patients with the *PLP1* missense mutation.

INTRODUCTION

Analysis of differentiated cells from disease-specific, human induced pluripotent stem cells (iPSCs) enables the construction of pathological models using the patients' own cells. Such analyses are particularly useful for the study of neurodegenerative disorders because it is difficult to collect brain-tissue samples from these patients.

Pelizaeus-Merzbacher disease (PMD) is a dysmyelinating disorder of the CNS that is usually observed during childhood. PMD is classified into two subtypes: the classical and connatal forms. In the classical form, patients usually show a delay in psychomotor development within the first year of life but exhibit relatively slow disease progression over the first decade. In contrast, in the connatal form, patients generally show arrested congenital psychomotor development and exhibit a progressive disease course with severe neurological impairment. The degree of dysmyelination has been shown to correlate well with the clinical severity of PMD (Seitelberger, 1995). The *proteolipid protein 1* (*PLP1*) gene has been identified as a causative gene for PMD. PLP1 is a transmembrane protein that is abundantly expressed in compact myelin in oligodendrocytes (OLs) and plays a structural role in the formation and maintenance of myelin sheaths (Gow et al., 1997; Mikoshiba et al., 1991). Three distinct types of *PLP1* mutation have been reported to date: point mutations, duplications, and deletions. Missense mutations in the *PLP1* gene account for 30% of the genetic abnormalities found in PMD patients and are responsible for most of connatal cases. Based on analyses using cell lines transfected with mutant *PLP1* genes (Gow and Lazzarini, 1996) or a mouse model of PMD (the *msd* mouse; Gow et al., 1998), the underlying pathogenesis in most patients with missense mutations is thought to involve the accumulation of misfolded mutant PLP1 proteins in the rough endoplasmic reticulum (ER) (Southwood et al., 2002) and the induction of ER stress, resulting in activation of the unfolded protein response (UPR). Although UPR attenuates general translation to reduce the protein load into ER and increase expression of chaperone proteins to facilitate protein folding, excessive levels of unfolded proteins have been shown to activate apoptotic pathway of UPR to eliminate damaged OLs.

Please cite this article in press as: Numasawa-Kuroiwa et al., Involvement of ER Stress in Dysmyelination of Pelizaeus-Merzbacher Disease with *PLP1* Missense Mutations Shown by iPSC-..., Stem Cell Reports (2014), http://dx.doi.org/10.1016/j.stemcr.2014.03.007

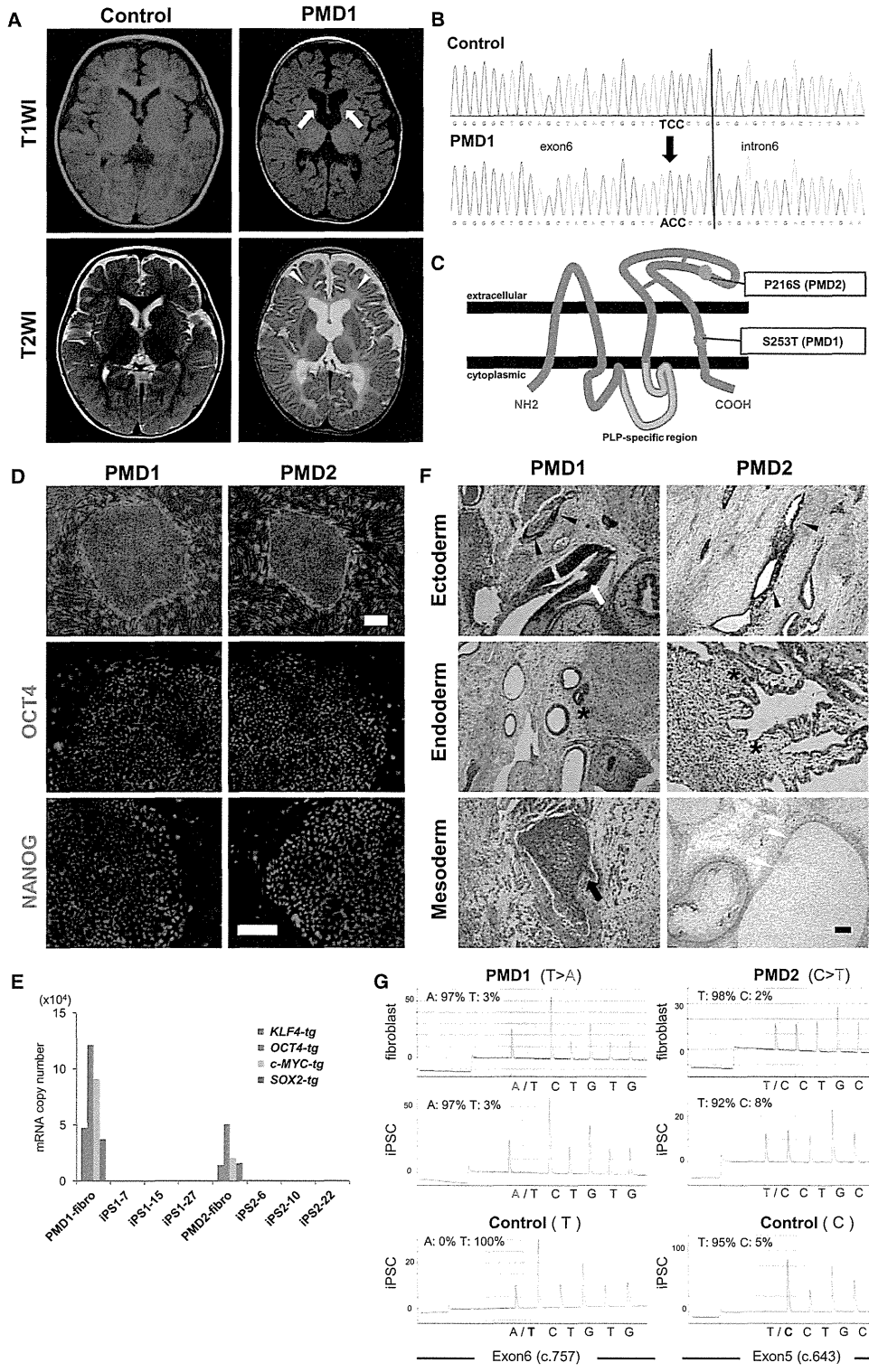

(legend on next page)

Please cite this article in press as: Numasawa-Kuroiwa et al., Involvement of ER Stress in Dysmyelination of Pelizaeus-Merzbacher Disease with *PLP1* Missense Mutations Shown by iPSC-..., Stem Cell Reports (2014), http://dx.doi.org/10.1016/j.stemcr.2014.03.007

However, despite the precise analyses conducted using conventional cellular and animal PMD models, it has not been possible to examine the actual correlation between the known molecular pathogenesis and cell biological phenotypes, including abnormalities in OL differentiation, myelination, and cell death. In addition, those previous results were obtained through analyses using nonhuman models, non-patient-derived cells, or nonoligodendrocyte models, and it is unknown whether the results obtained in those models are applicable to human patients. Although the establishment of iPSCs from a PMD patient with partial duplication of *PLP1* gene has been reported, those iPSCs were not differentiated into oligodendrocytes for disease modeling (Shimojima et al., 2012). Thus, in the present study, we focused on the pathologic effects of *PLP1* missense mutations and established patient-specific iPSCs from two PMD patients with different mutation sites and different levels of clinical severity.

We differentiated the iPSCs into OL lineage cells and examined the pathogenic changes in the PMD iPSC-derived OLs. We confirmed the accumulation and mislocalization of mutant PLP1 proteins to the ER, a high level of stress susceptibility, and increased apoptosis in PMD iPSC-derived OLs. In addition, through transmission electron microscopic analysis, we verified decreases in the frequency of myelin formation and the thickness of the myelin sheath compared with control cells. More importantly, we also demonstrated that these pathogenic changes observed in iPSC-derived OLs were consistent with the different levels of clinical severity between the two PMD patients. Thus, this report describes the modeling of human PMD with *PLP1* missense mutations using patient-specific, iPSC-derived OLs. These results have demonstrated the usefulness of iPSC-derived OLs for the analysis of the pathogenic processes in human dysmyelinating neurological disorders.

RESULTS

Clinical Features of PMD Patients

We established iPSCs from two patients with point mutations in the transmembrane domain (patient 1: PMD1) and extracellular domain (patient 2: PMD2) of the *PLP1* gene (Figure 1C). PMD1 was a 1-year-old male with the connatal form of PMD. He was diagnosed with PMD at the age of 4 months, when he was found to exhibit poor head control and nystagmus and was unable to follow objects. He showed poor feeding and was fed through a gastrostomy tube from the age of 21 months. Psychomotor development was not observed, even at the age of 5 years. MRI of the patient's brain revealed mild and diffuse atrophy, dilatation of the ventricles, and diffuse high-intensity signals in the white matter of the cerebrum and brainstem in a T2-weighted image (T2WI) (Figure 1A). A direct sequencing analysis of genomic DNA from the patient's leukocytes showed a novel missense mutation, c.757 T > A (p.Ser253Thr), in exon 6 of the *PLP1* gene (Figure 1B). This amino acid change has not been previously reported, but different type of mutation at this same site, Ser253Phe, has been reported in other patients with the connatal form of PMD (Hodes et al., 1998). This change was not identified in more than 200 normal individuals; thus, it was considered to be a causative mutation for PMD.

Patient 2 (PMD2) was a 20-year-old male with the classical form of PMD. He was diagnosed with PMD at the age of 3 months, when he was found to display poor head control and nystagmus. Spastic quadriparesis was evident at 4 years of age, with choreoathetotic movements beginning at the age of 8–10 years. He appeared alert and attentive and was nonverbal but exhibited guttural vocalizations. A missense mutation, c.643 C > T (p.Pro215Ser), was identified in exon 5 of the *PLP1* gene, which has been reported previously (Gencic et al., 1989).

Figure 1. Features of the PMD Patients and Characterization of iPSCs

(A) MRI images of the brains of patient PMD1 (right) and an age-matched control (left). Mild and diffuse atrophy of the brain, dilatation of the ventricles (arrow), and diffuse high-intensity signals in the white matter (arrowhead) are shown. T1WI, T1-weighted images; T2WI, T2-weighted images.

(B) Direct sequencing analysis of genomic DNA from PMD1's leukocytes showed a novel missense mutation c.757 T > A (p.Ser253Thr) in exon 6 of the *PLP1* gene.

(C) Schematic representation of the mutation sites in PMD1 and PMD2.

(D) Representative morphology of iPSC colonies (above) and immunochemical analysis of pluripotent markers, NANOG and OCT4 (below). The scale bars represent 200 μm.

(E) Quantitative RT-PCR analysis of the expression of retroviral transgenes in established PMD iPSC clones. Data are presented as the mRNA copy numbers for each transgene divided by those for *β-actin*.

(F) Representative H&E staining of teratomas derived from established PMD iPSC clones. Teratomas were formed via the injection of undifferentiated iPSCs into the testes of NOD/SCID mice. Open arrow, neural rosettes. Arrowhead, pigmented epitheliums. Asterisks, goblet cells. Arrow, bones. Open arrowhead, cartilage. The scale bars represent 200 μm.

(G) Representative pyrosequencing analysis of the mutations in the *PLP1* gene in fibroblasts and iPSCs. Identical mutations to those observed in the patients' fibroblasts (PMD1, 757 T > A; PMD2, 643 C > T) were confirmed in all the iPSC clones.

Please cite this article in press as: Numasawa-Kuroiwa et al., Involvement of ER Stress in Dysmyelination of Pelizaeus-Merzbacher Disease with *PLP1* Missense Mutations Shown by iPSC-..., Stem Cell Reports (2014), http://dx.doi.org/10.1016/j.stemcr.2014.03.007

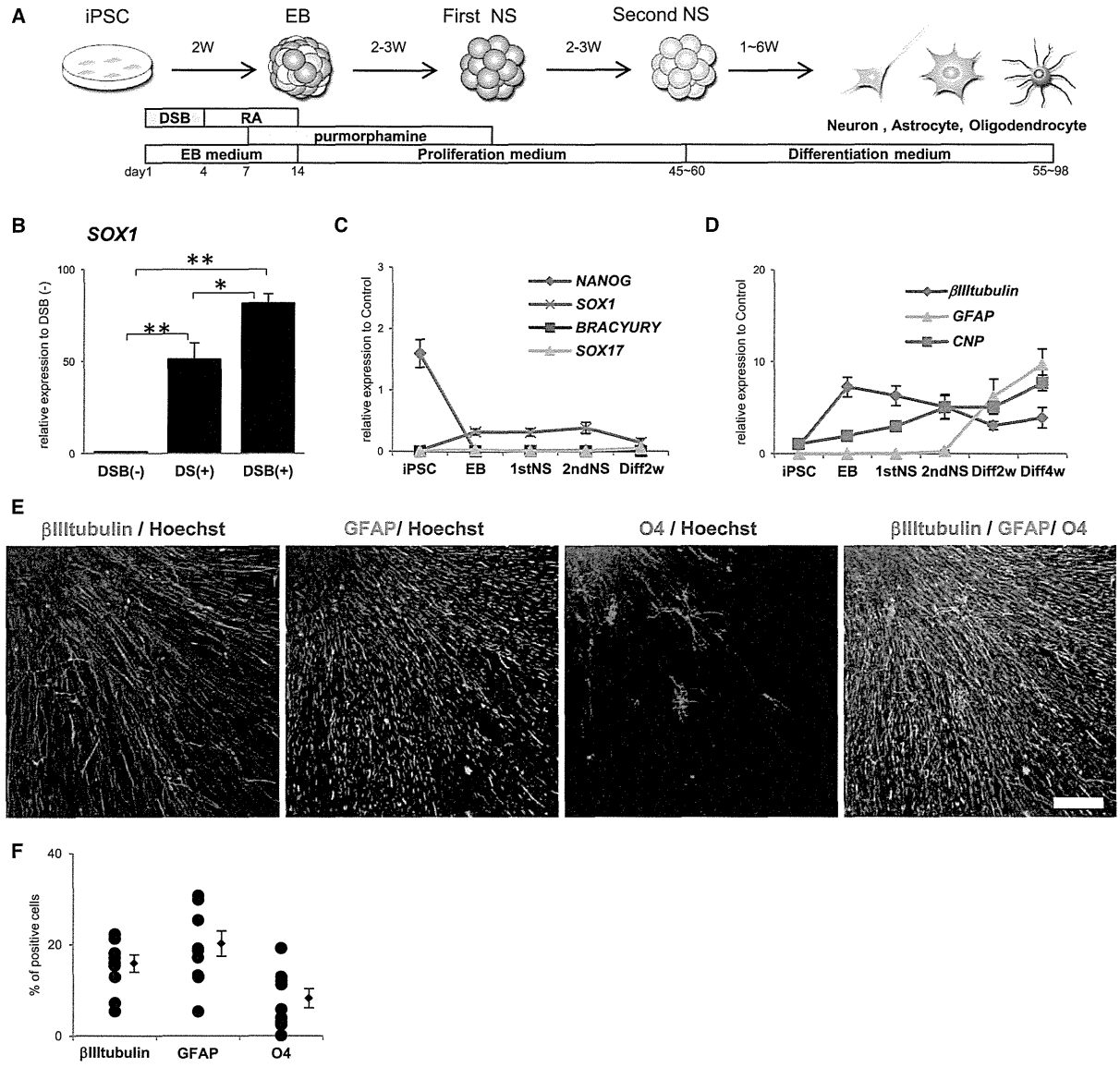

Figure 2. Differentiation Potential of Human iPSCs

(A) Schematic presentation of the protocols for OL differentiation from hiPSCs. DSB, dorsomorphine (D), SB431542 (S), and BIO (B); RA, retinoic acid; NS, neurospheres.

(B) Quantitative RT-PCR analysis of *SOX1* expression in EBs, suggesting a significantly higher induction efficiency of NS/PCs in EBs in our protocol with DSB (DSB: dorsomorphin, SB431542, and BIO) compared with those in our previously established methods (control, DSB−) or those in the previously reported method with dual Smad inhibition (DS) (n = 3, mean ± SEM; independent experiments; *p < 0.05; **p < 0.01; t test).

(C) Quantitative RT-PCR analysis of the expression of cell-type-specific markers at each differentiation stage. *NANOG* (a pluripotent marker) was readily downregulated in the EB stage. Other lineage markers (mesodermal and endodermal markers, such as *BRACHYURY* and *SOX17*) were not detected in any stage. *SOX1* was upregulated in EB and neurosphere stage in control iPSC clones (201B7, WD39, and TIG121; n = 3; mean ± SEM; independent experiments).

(D) Quantitative RT-PCR analysis of differentiated neurospheres for the markers of neurons (*βIII tubulin*), astrocytes (*GFAP*), and oligodendrocytes (*CNP*) in control iPSC clones (201B7, WD39, and TIG121; n = 3; mean ± SEM; independent experiments).

(legend continued on next page)

Establishment and Characterization of iPSCs Derived from PMD Patients

Human iPSCs were established via the retroviral transduction of four transcription factors (*SOX2*, *OCT4*, *KLF4*, and *c-MYC*) into dermal fibroblasts (Takahashi et al., 2007). A total of 52 and 34 iPSC clones were established from PMD1 and PMD2 samples, respectively. The established iPSC clones were evaluated based on the typical morphology of colonies similar to human embryonic stem cells (ESCs), as well as the expression of pluripotent markers via immunocytochemistry (NANOG and OCT4; Figure 1D), silencing of retroviral transgenes through quantitative RT-PCR (Figure 1E), and efficient differentiation into neural cells via embryoid body (EB) formation. We finally selected three clones each for PMD1 (1-7, 1-15, and 1-27) and PMD2 (2-6, 2-10, and 2-22) for further analyses. The differentiation potentials of these selected iPSC clones were confirmed through teratoma formation assays (ectoderm: neural rosettes and pigmented epithelium, endoderm: goblet cells, and mesoderm: bones and cartilage; Figure 1F). Moreover, the mutations in the *PLP1* gene (PMD1 [c.757 T > A] and PMD2 [c.643 C > T]) were confirmed in human dermal fibroblasts (HDFs) and all of the selected iPSC clones via pyrosequencing analysis (Figure 1G).

Regarding the control iPSCs, we used age-matched control iPSCs established from 8-month-old (TIG121) and 16-year-old (WD39) healthy individuals, corresponding to the PMD-iPSCs established from 1-year-old and 20-year-old patients, respectively, as well as 201B7, which is a widely used control iPSC clone.

Both Control and PMD iPSCs Induce Oligodendrocyte Lineage Cells In Vitro

Based on the previously reported methods for inducing OLs from human ESCs and iPSCs (Hu et al., 2009; Izrael et al., 2007; Kang et al., 2007), we established our own culture protocol to induce OLs by modifying previously established protocols for efficiently differentiating human ESCs and iPSCs into neural stem/progenitor cells (NS/PCs) as neurospheres through EB formation (Nori et al., 2011; Okada et al., 2008). First, dorsomorphin (a bone morphogenetic protein signal inhibitor), SB431542 (a transforming growth factor β [TGF-β] receptor inhibitor), and BIO (a GSK3 inhibitor) were added during the early phase of EB formation to facilitate differentiation into NS/PCs more efficiently. Quantitative RT-PCR analysis of the expression of the NS/PC marker *SOX1* in EBs revealed a significantly higher induction efficiency of NS/PCs in our protocol with DSB (DSB: dorsomorphin, SB431542, and BIO) compared with those in our previously established methods (control, DSB−) or those in the previously reported dual Smad inhibition with DS (Figure 2B). We also added retinoic acid for caudalization and purmorphamine (Sonic hedgehog agonist) for ventralization during EB formation until EB dissociation. Then, the dissociated EBs were cultured in suspension to form neurospheres in proliferation medium supplemented with factors that promote the commitment and proliferation of OL lineage cells (Shimada et al., 2012). For adherent differentiation, neurospheres were cultured in differentiation medium supplemented with factors that promote the commitment of OL lineage cells as indicated in the Experimental Procedures (Figure 2A). From the quantitative RT-PCR analysis in this protocol, the pluripotent marker (*NANOG*) was notably downregulated in the EB stage, and other lineage markers (mesodermal and endodermal markers, such as *BRACHYURY* and *SOX17*) were not detected in any stage. The NS/PC marker (*SOX1*) was upregulated in the EB and neurosphere stages and gradually downregulated after adherent differentiation (differentiation stage; Figure 2C). The expression profiles were similar between the control, PMD1, and PMD2 iPSCs (Figure S1A available online). To reveal the differentiation potentials of neurospheres, we performed immunocytochemistry of differentiated neurospheres for markers of neurons (βIII tubulin), astrocytes (GFAP), and oligodendrocytes (O4; Figures 2E and 2F) and a time course analysis of the expression levels of neuronal and glial markers through quantitative RT-PCR (Figure 2D). The expression profiles were similar between the control and PMD1 and PMD2 iPSCs (Figure S1B). Based on these analyses, we confirmed the differentiation potentials of the iPSCs into three neural lineage cells and the reproducibility of our differentiation protocol. Regarding the differentiation potentials of OL lineage cells, all PMD-iPSCs and control iPSCs were able to induce platelet-derived growth factor receptor α (PDGFRα)$^+$-OL progenitor cells (OPCs), O4$^+$-immature OLs (immature OLs), and myelin basic protein (MBP)$^+$-mature OLs (mature OLs) with typical morphologies (Figure 3B). OPCs were also positive for NG2 (Figure 3A). In contrast, myelin protein zero (MPZ)-positive cells, a major structural protein of peripheral myelin, could not be detected, indicating that these cells were oligodendrocytes, but not schwann cells.

After 55–70 days in vitro (DIV), OPCs were observed in 86.3% of the colonies of control cells and 95.1% and

(E) Representative low-magnification images of the immunocytochemistry of three neural lineage cells (neurons: βIII tubulin; astrocytes: GFAP; oligodendrocytes: 04). The scale bar represents 100 μm.
(F) Quantitative analysis of the percentages of three neural lineage cells in control-iPSCs (201B7, WD39, and TIG121)-derived neurospheres (n = 9; mean ± SEM; independent experiments).

Please cite this article in press as: Numasawa-Kuroiwa et al., Involvement of ER Stress in Dysmyelination of Pelizaeus-Merzbacher Disease with *PLP1* Missense Mutations Shown by iPSC-..., Stem Cell Reports (2014), http://dx.doi.org/10.1016/j.stemcr.2014.03.007

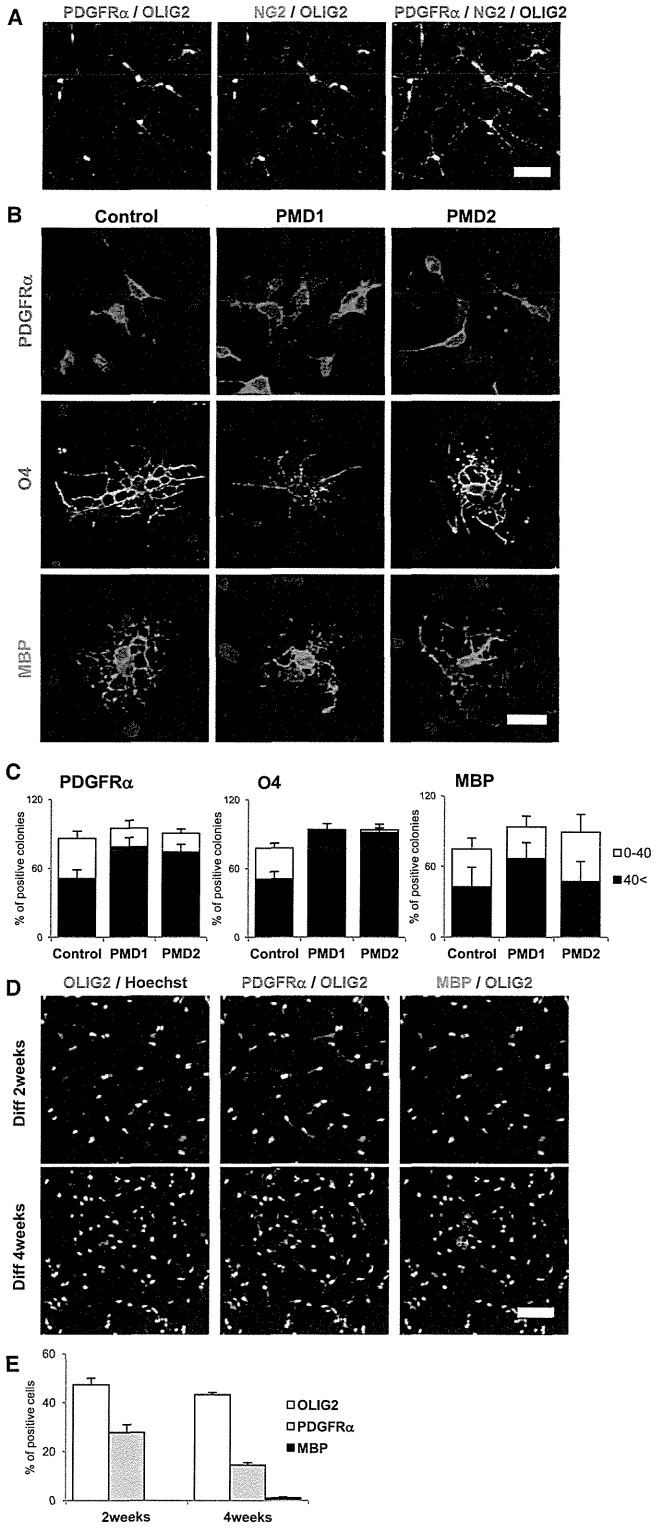

Figure 3. Differentiation Potential of Human iPSCs into Oligodendrocytes

(A) Representative image of immunocytochemistry for OPC markers (PDGFRα and NG2). OPCs were positive for both PDGFRα and NG2. The scale bar represents 50 μm.

(B) Representative image of immunocytochemistry of differentiated neurospheres using markers for OL lineage cells. Both control and PMD iPSCs differentiated into PDGFRα$^+$-OL progenitor cells (OPCs), O4$^+$-immature OLs (immature OLs), and MBP$^+$-mature OLs (mature OLs). The scale bar represents 20 μm.

(C) Quantitative analysis of the differentiation efficiency into OL lineage cells. The numbers of neurosphere colonies containing more than 40 marker-positive cells (≥40 cells; oligodendrocyte [++]), those containing less than 40 marker-positive cells (1–39 cells oligodendrocyte [+]), and those without marker-positive cells (oligodendrocyte [−]) were counted and are presented as the percentage of total neurosphere colonies. Oligodendrocyte (++) neurosphere colonies and oligodendrocyte (+) neurosphere colonies are indicated by black and white bars, respectively (PDGFRα, n = 6; O4, n = 6; MBP, n = 4; mean ± SEM; independent experiments). No significant difference was detected among control (201B7, WD39, and TIG121) and PMD iPSCs (PMD1-7, PMD1-15, and PMD1-27 and PMD2-6, PMD2-10, and PMD2-22)-derived OL lineage cells ($p > 0.05$; Mann-Whitney's U test).

(D) Representative image of immunocytochemistry for OLIG2, PDGFRα, and MBP after 2 or 4 weeks differentiation of control-iPSC-derived second neurospheres containing more than 40 OLIG2-positive cells. The scale bar represents 50 μm.

(E) Quantitative data of the percentages of PDGFRα$^+$ cells/OLIG2$^+$ cells and MBP$^+$ cells/OLIG2$^+$ cells (after 2 or 4 weeks of differentiation) in control-iPSC (201B7, WD39, and TIG121)-derived neurospheres containing more than 40 OLIG2-positive cells. (n = 3; mean ± SEM; independent experiments). After 2 and 4 weeks of differentiation, OLIG2$^+$ and PDGFRα$^+$ OPCs were abundantly observed. After 4 weeks of differentiation, small numbers of MBP$^+$ mature OLs appeared.

Please cite this article in press as: Numasawa-Kuroiwa et al., Involvement of ER Stress in Dysmyelination of Pelizaeus-Merzbacher Disease with *PLP1* Missense Mutations Shown by iPSC-..., Stem Cell Reports (2014), http://dx.doi.org/10.1016/j.stemcr.2014.03.007

90.5% of the colonies of PMD1 and PMD2 cells, respectively. At 70–85 DIV, immature OLs were observed in 77.8% of control colonies and 93.8% and 93.8% of the colonies of PMD1 and PMD2 cells, respectively. At 80–95 DIV, mature OLs were observed in 74.9% of the colonies of control cells and 93.8% and 89.2% of the colonies of PMD1 and PMD2 cells, respectively (Figure 3C). No significant differences were detected in either control or PMD with regard to OL lineage differentiation efficiency.

To examine the proportion of immature and mature OL lineage cells, we performed immunocytochemistry for OLIG2, PDGFRα, and MBP after 2 or 4 weeks differentiation of control-iPSC-derived second neurospheres containing more than 40 OLIG2-positive cells and counted the number of marker-positive cells (Figures 3D and 3E). After 2 and 4 weeks of differentiation, $OLIG2^+$ and $PDGFR\alpha^+$ OPCs were abundantly observed. After 4 weeks of differentiation, small numbers of MBP^+ mature OLs appeared.

Involvement of ER Stress in PMD

Previous in vitro transfection studies in nonglial cells have indicated that various PLP1 mutants accumulate in the ER immediately after translation, in contrast to the distribution of wild-type PLP1 at the plasma membrane (Gow et al., 1994; Gow and Lazzarini, 1996; Thomson et al., 1997). Therefore, we next examined the expression of PLP1 proteins via immunocytochemistry. When stained with anti-PLP1 and MBP antibodies, the membrane protein PLP1 was observed to be dispersed into the processes of OLs and to colocalize with MBP in control iPSC-derived mature OLs. However, in PMD1 and PMD2 iPSC-derived mature OLs, PLP1 protein staining was not observed in the OL processes; instead, PLP1 protein staining localized to the perinuclear cytoplasm (Figure 4A). Thus, we also performed staining for the ER marker KDEL and found that the mislocalized PLP1 proteins colocalized with KDEL (Figures 4A and 4B). All of the control iPSC-derived OLs showed staining for PLP1 proteins in the processes of mature OLs, whereas all of the PMD iPSC-derived mature OLs only exhibited PLP1 protein localization in the ER. These results suggest that mutant PLP1 proteins accumulated in the ER and triggered ER stress in mature OLs derived from PMD-iPSCs.

We next examined the expression of ER stress markers in OLs. $O4^+$ cells were isolated from both the PMD and control iPSC-derived differentiated cells 4 weeks after the attachment of the second neurospheres via magnetic-activated cell sorting (MACS) using an anti-O4 antibody. The purified $O4^+$ cells underwent quantitative RT-PCR to determine the expression of ER stress markers (*BIP*, *CHOP*, and spliced *XBP1*). No significant differences were detected between the control and PMD iPSC-derived OLs regarding the expression of ER stress markers under default conditions (Figure 4C). Therefore, we next examined the susceptibility of the iPSC-derived OLs to the extrinsic ER stress induced by treatment with a low concentration of tunicamycin 50 nM for 6 hr (known as an ER-stress inducer). The results showed that the expression of all ER-stress markers was significantly increased in tunicamycin-treated $O4^+$ cells relative to untreated $O4^+$ cells in PMD1 (Figure 4D). This result suggested that a higher susceptibility to ER stress was observed in PMD1 iPSC-derived OLs than in those derived from control and PMD2 iPSCs.

We next treated the iPSC-derived OLs with a higher concentration of tunicamycin 100 nM for 6 hr and examined the expression levels of ER stress markers. PMD2 iPSC-derived OLs showed significantly higher expression levels of spliced *XBP1*, the most sensitive ER stress marker, than control iPSC-derived OLs (Figure 4E). No significant differences were detected in the expression levels of *BIP* and *CHOP* between control and PMD2. Taken together, these results suggest that ER stress is involved in the pathogenesis of the PMD patients with PLP1 missense mutations, and a higher susceptibility to ER stress was observed in PMD1 iPSC-derived OLs than in those derived from PMD2, which is consistent with the more severe phenotypes of the PMD1 patient compared with the PMD2 patient.

Increased Apoptosis Is Observed in PMD iPSC-Derived Oligodendrocytes

In addition to their susceptibility to ER stress, the PMD iPSC-derived OLs showed significant morphological differences, as revealed by O4 staining, such as scattered O4 staining in their processes compared with control iPSC-derived OLs, which exhibited uniform O4 staining in their processes (Figure 5A). Thus, to investigate the apoptotic processes of PMD iPSC-derived OL lineage cells, we examined the expression of cleaved caspase-3 (apoptotic marker) in $O4^+$-immature OLs and MBP^+-mature OLs via immunostaining. Some of the PMD iPSC-derived OLs that showed scattered O4 staining in their processes were positive for cleaved caspase-3 (Figure 5B). The numbers of cleaved caspase-3^+ cells in both PMD1 and PMD2 iPSC-derived immature OLs and mature OLs were significantly increased compared with those derived from control iPSCs (Figure 5C). We next performed immunocytochemistry for KI67 and OLIG2. We found that the proportion of $OLIG2^+$ cells and $KI67^+$ cells among $OLIG2^+$ cells were unchanged between PMD and control samples, suggesting that the compensatory proliferation of OPCs for increased apoptosis in PMD iPSC-derived OLs is unlikely (Figures S2A and S2B). Therefore, although the differentiation efficiency into oligodendrocyte lineage cells was unchanged between PMD and control (Figure 3C), considering that anti-O4 and anti-MBP antibodies stain both apoptotic and live OLs (Figures 5A and 5C), the increased levels of apoptosis resulted in decreased numbers of live OLs in PMD iPSC-derived cultures.

Please cite this article in press as: Numasawa-Kuroiwa et al., Involvement of ER Stress in Dysmyelination of Pelizaeus-Merzbacher Disease with *PLP1* Missense Mutations Shown by iPSC-..., Stem Cell Reports (2014), http://dx.doi.org/10.1016/j.stemcr.2014.03.007

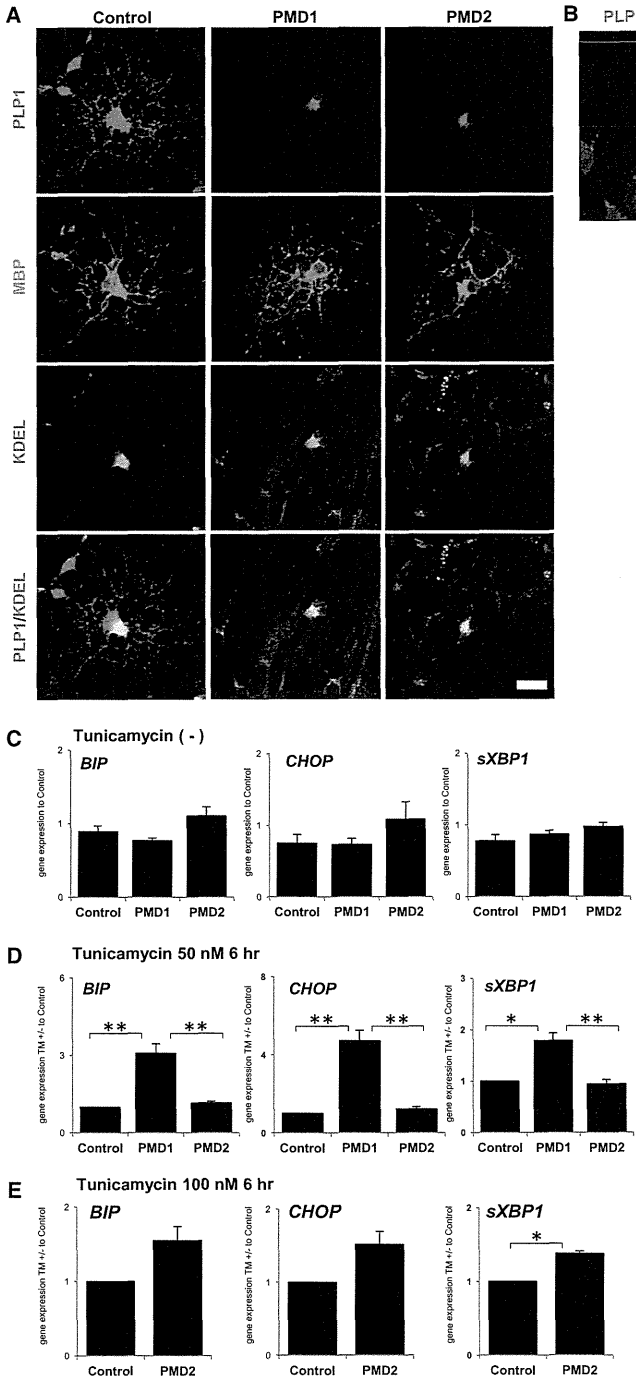

Figure 4. Involvement of ER Stress in PMD-Derived Oligodendrocytes

(A) Representative immunocytochemistry image for PLP1, the OL marker MBP, and the ER marker KDEL. In the control iPSC-derived mature OLs, the PLP1 protein localized to both the ER (KDEL) and membrane, whereas in the PMD iPSC-derived OLs, the mutant PLP1 protein only localized to the ER. The scale bar represents 20 μm.

(B) Three-dimensional image of mature OLs derived from PMD1 iPSCs showing colocalization of the mutant PLP1 protein and KDEL via confocal laser scanning microscopy. The scale bars represent 20 μm.

(C) Quantitative RT-PCR analyses of the expression of ER stress markers in $O4^+$ cells. The data are presented as the expression relative to that in iPSCs. No significant differences were observed between the control iPSC (201B7, WD39, and TIG121) and PMD iPSC (PMD1-7, PMD1-15, and PMD1-27 and PMD2-6, PMD2-10, and PMD2-22)-derived cells (n = 5; mean ± SEM; independent experiments; t test).

(D) Quantitative RT-PCR analyses of the expression of ER stress markers in tunicamycin-treated (50 nM; 6 hr) $O4^+$ cells relative to untreated $O4^+$ cells. A higher level of stress susceptibility was detected in PMD1 (PMD1-7, PMD1-15, and PMD1-27) than in control (201B7, WD39, and TIG121) and PMD2 (PMD2-6, PMD2-10, and PMD2-22; n = 5; mean ± SEM; independent experiments; *p < 0.05; **p < 0.01; Mann-Whitney's U test).

(E) Quantitative RT-PCR analyses of the expression of ER stress markers in tunicamycin-treated (100 nM; 6 hr) $O4^+$ cells relative to untreated $O4^+$ cells. PMD2 iPSC (PMD2-6, PMD2-10, and PMD2-22)-derived OLs showed significantly higher expression levels of spliced *XBP1* than control iPSC (201B7, WD39, and TIG121)-derived OLs (n = 3; mean ± SEM; independent experiments; *p < 0.05; t test).

Because previous reports have indicated the neurotrophic actions of PLP1 (Griffiths et al., 1998; Yin et al., 2006), we next investigated whether apoptosis was induced in PMD patient-derived neurons. However, no cleaved caspase-3^+ neurons derived from either control or PMD iPSCs were observed (Figure S2C), suggesting that this increased apoptosis was specific to oligodendrocyte lineage cells in PMD in our iPSC-derived cultures.

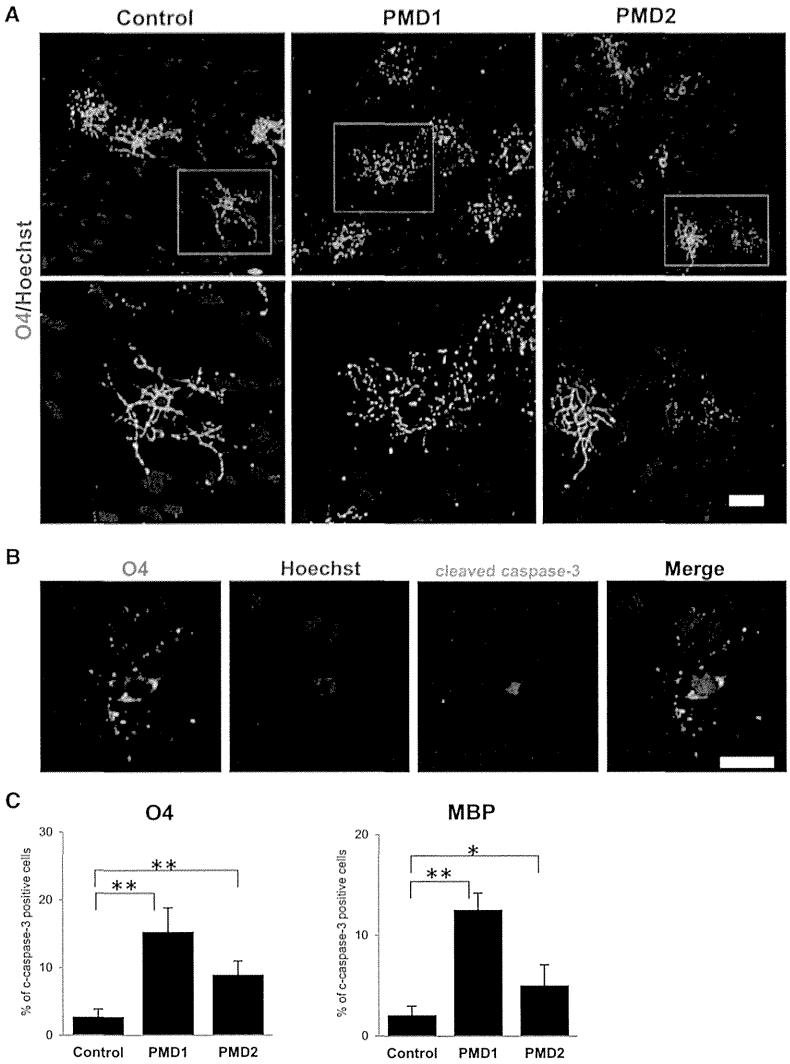

Figure 5. Enhanced Apoptosis in PMD iPSC-Derived Oligodendrocytes

(A) Morphological differences in OLs. Immunocytochemical analysis of iPSC-derived OLs for OLs marker (O4) and nuclei (Hoechst). The OLs showed a uniform appearance in the control iPSC-derived cells but showed scattered morphologies in the PMD iPSC-derived cells. The scale bar represents 40 μm.

(B) Representative immunocytochemical images of apoptotic OLs using markers for apoptosis (cleaved caspase-3) and OLs (O4). OLs ($O4^+$ or MBP^+) that were both positive for cleaved caspase-3 and showed nuclear condensation or fragmentation were considered apoptotic OLs. The scale bar represents 40 μm. c-caspase-3, cleaved caspase-3.

(C) Quantitative analysis of the number of apoptotic OLs. The number of apoptotic cells was higher in the PMD1 (PMD1-7, PMD1-15, and PMD1-27) and PMD2 iPSC (PMD2-6, PMD2-10, and PMD2-22)-derived OLs than control iPSC (201B7, WD39, and TIG121)-derived OLs (n = 9; mean ± SEM; independent experiments; *p < 0.05; **p < 0.01; Mann-Whitney's U test).

Abnormal Myelin Structures and ER Morphologies Were Detected by Electron Microscopic Analysis

Finally, we focused on the myelinating properties of PMD iPSC-derived OLs, which represent the most characteristic pathogenic feature of PMD. Because different types of neural cells, including neurons and astrocytes, in addition to OLs, were derived in our cultures, neuron-glial interactions could be observed and neuron myelination by the iPSC-derived OLs could be analyzed in situ. In immunocytochemical analysis of MBP and NF200 (neurofilament marker), parts of the neurofilament$^+$ neurites were wrapped by the MBP^+ process of iPSC-derived oligodendrocytes (Figure S3A). Thus, to evaluate the histological abnormality of the myelin structures in vitro, we performed transmission electron microscopy (TEM) analysis of ultrathin sections of the differentiated cells. The results showed that myelin structures with or without axons could be observed via TEM. Considering the neuronal processes wrapped by the MBP^+ process of iPSC-derived OLs observed through immunocytochemistry, some of the axonal structures could have been lost during the fixation process for TEM. Although we stained with antibodies against NAV1.6 (nodes) and CASPER (paranodes), we could not detect any significant staining in our cultures. This may suggest immature myelination in the present culture conditions.

Notably, mature myelin structures with thick myelin lamella ~30 layers were observed in the control cultures. In contrast, in the PMD iPSC-derived cultures, a limited

Please cite this article in press as: Numasawa-Kuroiwa et al., Involvement of ER Stress in Dysmyelination of Pelizaeus-Merzbacher Disease with *PLP1* Missense Mutations Shown by iPSC-..., Stem Cell Reports (2014), http://dx.doi.org/10.1016/j.stemcr.2014.03.007

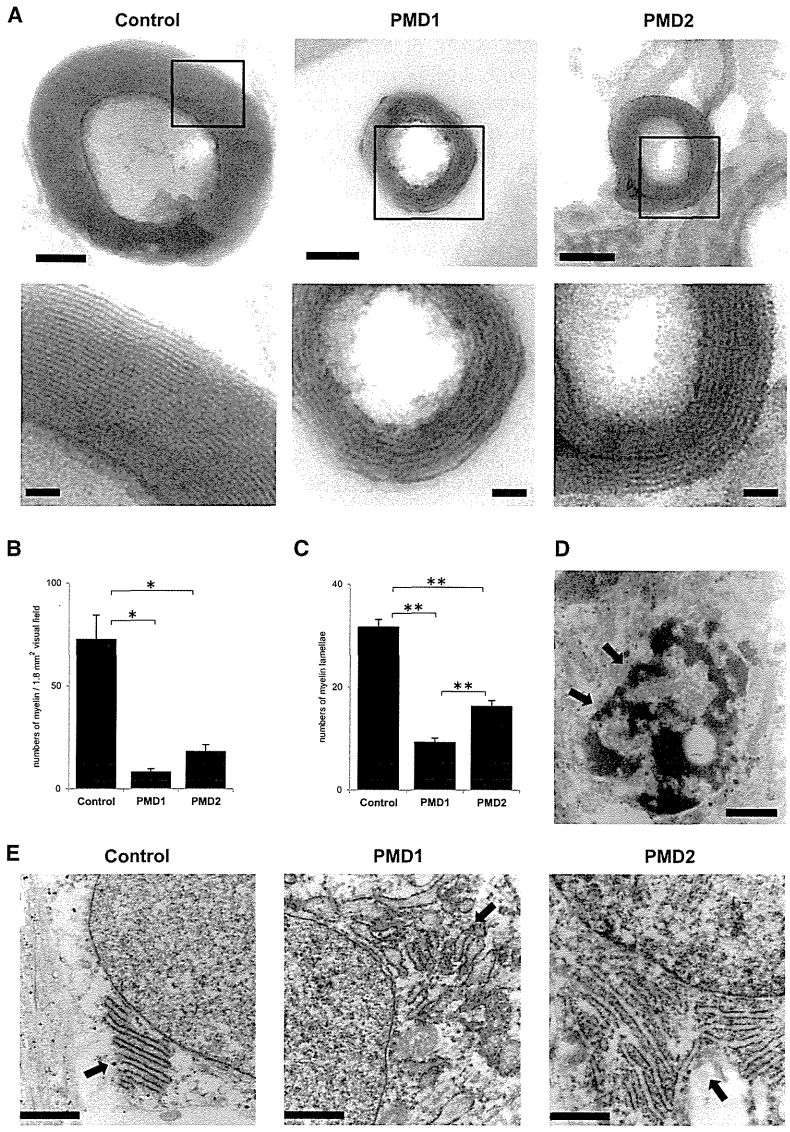

Figure 6. Electron Microscopic Analysis of PMD iPSC-Derived Cells

(A) TEM of iPSC-derived cells. The maximum number of normal myelin lamella was greater than 30 in the control iPSC-derived myelin sheaths. In contrast, a limited number of myelin lamella was observed in the PMD iPSC-derived myelin sheaths. High-magnification images are also shown in the lower panel. The scale bars represent 100 nm (upper panels) and 20 nm (lower panels).

(B) Quantitative analysis of the numbers of myelin structures. We counted the numbers of myelin structures per visual field of EM images (approximately 1.8 mm^2) for the myelination frequency. The frequency of myelin formation was significantly decreased in both PMD1 (PMD1-7, PMD1-15, and PMD1-27) and PMD2 (PMD2-6, PMD2-10, and PMD2-22) iPSC-derived OLs (n = 3; mean ± SEM; independent experiments; *p < 0.05; t test).

(C) Quantitative analysis of the numbers of myelin lamellae. We counted the numbers of major dense lines per myelinated fiber for the thickness of myelin, and the average of the numbers of myelin lamellae in the top ten myelin sheaths are presented. The thickness of the myelin sheath was greatly reduced in both PMD1 (PMD1-7, PMD1-15, and PMD1-27) and PMD2 (PMD2-6, PMD2-10, and PMD2-22) iPSC-derived OLs (n = 3; mean ± SEM; independent experiments; **p < 0.01; t test).

(D and E) Histological abnormalities detected in PMD iPSC-derived cells via TEM. Apoptotic cells with fragmented nuclei (arrow in D) were frequently detected among the PMD-iPSC-derived cells (D). The scale bar represents 1 μm. Dilations of ER intermembrane spaces were also observed (E). The scale bars represent 0.5 μm.

number of myelin structures with thin myelin lamella ~15 layers were observed (Figure 6A). The frequency of myelin formation and thickness of the myelin sheath were significantly decreased in both PMD1 and PMD2 iPSC-derived OLs (Figures 6B and 6C).

In addition, several types of histological abnormalities were detected in the PMD cells. Apoptotic cells exhibiting nuclear condensation were frequently observed among the PMD iPSC-derived cells, in contrast to that observed in those derived from control iPSCs (Figure 6D). Moreover, aberrant ER morphologies, such as dilation of the ER intermembrane space (Fan et al., 2013; Lim et al., 2011), were found in the PMD iPSC-derived cells (Figure 6E). These results indicate that PMD iPSC-derived OLs develop a poor myelin structure and subsequently die, supporting the involvement of ER stress in the pathogenesis of PMD.

DISCUSSION

In this study, we established PMD-specific human iPSCs from two patients with different clinical severity and different missense mutations of *PLP1*. One mutation is in the transmembrane domain (PMD1) and the other is in

Please cite this article in press as: Numasawa-Kuroiwa et al., Involvement of ER Stress in Dysmyelination of Pelizaeus-Merzbacher Disease with *PLP1* Missense Mutations Shown by iPSC-..., Stem Cell Reports (2014), http://dx.doi.org/10.1016/j.stemcr.2014.03.007

the extracellular domain (PMD2), both of which differ from those in the previously reported PMD animal models. And we generated patient-specific OLs. This model enables an investigation of the correlations between the molecular pathophysiology of PMD and various cell biological phenomena, including OL differentiation, myelination, and apoptosis in patient-derived live OLs through morphological, biochemical, and molecular biological methods. These analyses could not be achieved using conventional disease models.

Although there are several reported methods for inducing OPCs from human ESCs (Hu et al., 2009; Izrael et al., 2007; Kang et al., 2007), these methods have difficulties in reproducibility, making it difficult to obtain sufficient amounts of mature OLs for analysis. In the present study, we developed an improved neural differentiation protocol for human pluripotent stem cells by utilizing an EB-neurosphere method involving dual Smad inhibition in combination with a GSK3 inhibitor to facilitate differentiation into NS/PCs more efficiently and reproducibly. In addition, the use of T3, ciliary neurotrophic factor (CNTF), and leukemia inhibitory factor (LIF) was beneficial for differentiation into OLs. Using this method, we achieved stable differentiation of several human iPSC clones into OLs in a similar manner to that reported in a recent study (Wang et al., 2013). Remarkably, our culture procedure enabled recapitulation of myelin formation in human iPSC (hiPSC)-derived neurites and OLs in vitro in a single-culture system without coculturing with other cells, such as rodent hippocampal neurons, as previously reported (Kang et al., 2007). Thus, this study reports a successful in vitro myelination assay using human iPSC-derived neurons and OLs.

Another important finding of this study was that the differentiation of PMD iPSCs into OLs well-recapitulated the progression of PMD pathogenesis in vitro. Although the PMD-specific iPSCs induced abundant MBP^+ mature OLs, myelination was substantially less frequent and limited lamella formation was observed. These results suggest that incomplete maturation and limited survival of OLs rather than a failure to differentiate into OLs is responsible for PMD pathogenesis. However, the cause of OL degeneration and dysmyelination observed in PMD is unclear. Some previous reports have demonstrated the involvement of ER stress in the pathogenesis of PMD associated with missense mutations in the *PLP1* gene. Analyses using cell lines, such as cos7 cells transfected with wild-type or mutant *PLP1* genes, have shown that wild-type PLP1 protein is synthesized in the ER and transported to the cell surface, whereas mutant PLP1 proteins are arrested in the secretory pathway at an early stage and accumulate in the ER (Gow et al., 1994). In the CNS of PMD model mice, such as msd and rsh mice, mutant PLP1 proteins are largely confined to the perinuclear region of OLs and involved in the UPR (Gow et al., 1998). These reports suggest the involvement of ER stress in PMD pathogenesis. In the present study, accumulation of misfolded mutant PLP1 proteins in the ER and high susceptibility to ER stresses in the PMD1 and PMD2 cells were observed. This increased susceptibility to ER stresses or other cellular response could have resulted in the apoptosis of PMD iPSC-derived OLs and immature/incomplete myelination.

In addition, we detected differences between PMD1 and PMD2 cells. The differences of susceptibility to ER stresses and the thickness of the myelin sheath were consistent with the different levels of clinical severity of the two patients. The correlations between different clinical severity, different missense mutations, and different pathogenic changes have not previously been reported by conventional disease models. These results suggest that this PMD model accurately recapitulates disease pathophysiology not only qualitatively but also in terms of the degree of disease progression, although how the different point mutations affect the degree of the observed phenotype must be clarified. Accordingly, we propose models for a "proof-of-concept" of PMD pathogenesis based on the endogenous mutations found in PMD iPSC-derived OLs. The present findings cannot be generalized to PMD as a whole because the more common *PLP1* duplication was not included; therefore, we will investigate the pathogenesis of PMD with *PLP1* duplications in the future.

The current study represents the a demonstration of pathogenic changes in PMD patients with *PLP1* missense mutations using disease-specific, human iPSC-derived OLs. This model faithfully reproduces the pathophysiology observed in the CNS of PMD patients, which is difficult to identify through conventional experiments. Moreover, our results demonstrate the usefulness of iPSC-derived OLs for the analysis of the pathogenic processes of dysmyelinating human neurological disorders and the development of novel therapeutic agents for their treatment.

EXPERIMENTAL PROCEDURES

Isolation of Human Skin Fibroblasts and Generation of iPSCs

HDFs from the dermis of a 1-year-old Japanese male patient and HDFs from the dermis of a 20-year-old Caucasian male patient (Coriell Institute) were used to establish PMD1-iPSCs (PMD1-7, 1-15, and 1-27) and PMD2-iPSCs (PMD2-6, 2-10, and 2-22), respectively. Additional control cell lines used in this study included 201B7 (control A, established from HDFs [Cell Applications] from the dermis of a 36-year-old Caucasian female; Takahashi et al., 2007), WD39 (control B, established from HDFs from the dermis of a 16-year-old Japanese female; Imaizumi et al., 2012), and TIG121 (control C, established from HDFs from the dermis

of an 8-month-old Japanese male [Japan Health Sciences Foundation]). All of the human iPSC clones were established through the retroviral transduction of four transcription factors (*SOX2*, *OCT4*, *KLF4*, and *c-MYC*) into HDFs as described previously (Takahashi et al., 2007) and evaluated based on the expression of pluripotent markers, the silencing of retroviral transgenes, and teratoma formation assays as described previously (Ohta et al., 2011). We used three clones for each group for further analysis: control (201B7, WD39, and TIG121), PMD1 (1-7, 1-15, and 1-27), and PMD2 (2-6, 2-10, and 2-22). The data from the three clones were combined in each figure, and the data are shown as the average of the three clones. All of the experimental procedures for iPSC production were approved by the ethics committee of the Keio University School of Medicine (approval number: 20-16-18).

Culture and In Vitro Differentiation of Human iPSCs

hiPSCs were grown on mitomycin-C-treated SNL murine fibroblast feeder cells in gelatin-coated (0.1%) tissue culture dishes. The hiPSCs were maintained in standard hESC medium (Dulbecco's modified Eagle's medium [DMEM]/F12 [Sigma] containing 20% KnockOut serum replacement [KSR; Life Technologies], nonessential amino acids [NEAA], 0.1 mM 2-mercaptoethanol [Sigma], and 4 ng/ml fibroblast growth factor 2 [FGF-2] [PeproTech]) at 37°C in a humidified atmosphere of 3% CO_2.

For in vitro differentiation, iPSC colonies were detached from the feeder layers en bloc using a dissociation solution (0.25% trypsin, 100 μg/ml collagenase IV [Invitrogen], 1 mM $CaCl_2$, and 20% KSR; day 0) and cultured in suspension in bacteriological dishes to form EBs in a humidified atmosphere of 3% CO_2. From day 1 to 4 of EB formation, 3 μM dorsomorphin (Sigma), 3 μM SB431542 (Tocris Bioscience), and 3 μM BIO ((2′Z, 3′E)-6-bromoindirubin-3′-oxime; Sigma) were added. In addition, 1 μM retinoic acid (Sigma) and 1 μM purmorphamine (Calbiochem) were added on days 4 and 7, respectively, and maintained thereafter until day 16 (EB dissociation). The medium was changed every 2 days. On day 16, the EBs were enzymatically dissociated into single cells using TrypLE Select (Life Technologies), and the dissociated cells were cultured in suspension at a density of 1×10^5 cells/ml in proliferation medium consisting of serum-free medium (media hormone mix [MHM]; Okada et al., 2008) supplemented with 2% B27 supplement (Invitrogen), NEAA, 1 μM purmorphamine, 60 ng/ml T3 (Sigma), 10 ng/ml PDGF-AA (PeproTech), 20 ng/ml FGF, 10 ng/ml epidermal growth factor (PeproTech), 10 ng/ml insulin growth factor 1, and 10 ng/ml neurotrophin-3 (R&D Systems) in a humidified atmosphere of 5% CO_2. The medium was changed every 4~6 days for approximately 15~20 days to form the first neurospheres. To passage neurospheres, the first neurospheres were dissociated in the same manner as described above and cultured at a density of 1×10^5 cells/ml in proliferation medium without purmorphamine for approximately 15~20 days. To assay neurosphere differentiation, undissociated 5–7 neurospheres were plated onto coverslips 10 mm in diameter coated with poly-L-ornithine (Sigma) and growth-factor-reduced Matrigel (50× dilution, thin coated; Invitrogen), and cultured in differentiation medium that consisted of MHM supplemented with 2% B27 supplement, NEAA, 60 ng/ml T3, 10 ng/ml hLIF (Millipore), and 25 ng/ml CNTF (R&D Systems) for 2–6 weeks in a humidified atmosphere of 5% CO_2. Half of the medium was changed every 2 or 3 days. For the quantitative analysis of the differentiation efficiency into OL lineage cells, the numbers of neurosphere colonies containing more than 40 marker-positive cells (≥40 cells, oligodendrocyte [++]), those containing less than 40 marker-positive cells (1–39 cells, oligodendrocyte [+]), and those without marker-positive cells (oligodendrocyte [−]) were counted and are presented as the percentage of total neurosphere colonies. To examine the expression of ER-stress markers, $O4^+$ differentiated cells were purified 4 weeks after the attachment of the neurospheres using MACS technology with an anti-O4 antibody.

Direct Sequencing and Pyrosequencing Analysis of the *PLP1* Gene

Genomic DNA was extracted from peripheral blood samples (leukocytes) from PMD1 and from HDFs and iPSCs from both PMD1 and PMD2. For direct sequencing of the mutations in the *PLP1* gene in PMD1, fragments of the promoter regions (5′ UTR) and all seven exons of the *PLP1* gene were amplified via PCR. The PCR primers and cycling conditions employed for direct sequencing are listed in Table S1. For pyrosequencing analysis of the mutations in the *PLP1* gene in HDFs and iPSCs, fragments containing the PMD1 mutation (c.757 T > A in exon 6) and PMD2 mutation (c.643 C > T in exon 5) were amplified via PCR using forward primers and biotinylated reverse primers. Pyrosequencing analyses were performed following the manufacturer's instructions (Pyromark Q24; QIAGEN). The PCR primers and cycling conditions applied for pyrosequencing analysis are listed in Table S2.

RNA Isolation and RT-PCR

RNA isolation and real-time quantitative RT-PCR were performed as previously described using SYBR Premix ExTaq II and the MX3000P Real-Time PCR system (Stratagene; Okada et al., 2004, 2008). The amount of cDNA was normalized to that of human-specific *β-ACTIN* mRNA.

For the analysis of the expression of retroviral transgene in iPSCs, HDFs 7 days after the retroviral introduction (day 11 of the protocol) of four genes (*SOX2*, *OCT4*, *KLF4*, and *c-MYC*) were used as the positive control (*SOX2* tg, *OCT4* tg, *KLF4* tg, and *c-MYC* tg). The data are presented as the copy numbers of mRNA for each transgene. As for the analyses of *NANOG*, *SOX1*, *BRACHYURY*, *SOX17*, *βIII tubulin*, *GFAP*, *CNP*, and ER stress marker (*BIP*, *CHOP*, and *spliced XBP1*), data are presented as the relative expression to that in control. The applied primer sequences and PCR cycling conditions are listed in Table S3.

Immunocytochemical Analysis

For immunocytochemical analysis, cells were fixed with 4% paraformaldehyde for 30 min at room temperature. After blocking in blocking buffer (PBS containing 10% normal goat or donkey serum and 0.3% Triton X-100) for 1 hr at room temperature, the cells were incubated with primary antibodies at 4°C overnight. For O4 staining, we used blocking buffer without Triton X-100. After three washes with PBS, the cells were incubated with Alexa 488-, Alexa 555-, or Alexa 647-conjugated secondary antibodies (Life Technologies) for 1 hr at RT. Nuclei were stained with 10 μg/ml Hoechst 33258 (Sigma). After washing with PBS, the cells were mounted

on slides and examined with a universal fluorescence microscope (Axiophoto; Carl Zeiss) or confocal laser scanning microscope (LSM700; Carl Zeiss). The primary antibodies used in these analyses were as follows: NANOG (1:100; ReproCELL), OCT4 (1:500; Santa Cruz Biotechnology), OLIG2 (1:1,000; R&D Systems), PDGFRα (1:2,000; Santa Cruz Biotechnology), NG2 (1:2,000; Millipore), O4 (1:5,000; Millipore), MBP (1:1,000; Serotec), β-III-tubulin (1:1,000; Sigma), NF200 (1:1,000, Millipore), GFAP (1:4,000, Dako), KDEL (Abcam), PLP1 (1:30,000; gifted from Inoue; recognizes PLP1, but not DM20), KI67 (1:10,000, Abcam), and cleaved caspase 3 (1:1,000, Cell Signaling Technology).

Teratoma Assay

Undifferentiated iPSCs (5×10^5 cells) were injected into the testes of 8-week-old male nonobese diabetic (NOD)/severe combined immunodeficiency (SCID) mice (Charles River Laboratories) as described previously (Ohta et al., 2011). Eight weeks after injection, the resultant tumors were dissected and fixed with 4% paraformaldehyde. Paraffin-embedded tissue sections were produced, and hematoxylin and eosin (H&E) staining was performed. Images were obtained using a BZ-9000 microscope (Keyence).

Transmission Electron Microscopy

For TEM analysis, neurospheres and cells in dishes were fixed with 2.5% glutaraldehyde in 50 mM phosphate buffer (PB) overnight at 4°C. After washing twice in 0.1 M PB, these samples fixed with 1% osmium tetroxide for 90 min, dehydrated through ethanol, and embedded in Epon. The neurospheres were dissected and fixed on the stage, followed by the preparation of ultrathin sections with a thickness of 70 nm using an ultramicrotome (Leica Microsystems). The sections were subsequently stained with uranyl acetate and lead citrate for 10 and 12 min, respectively. Finally, the sections were observed under a transmission electron microscope (JEOL model 1230), and images were captured with Digital Micrograph 3.3 (Gatan). For the quantitative analysis of myelination, the number of myelin lamellae, which is the number of major dense lines per myelinated fibers, was counted to assess myelin thickness and the number of myelinated fibers per visual field of electron microscopy (EM) images (approximately 1.8 mm^2) was counted to assess myelination frequency.

SUPPLEMENTAL INFORMATION

Supplemental Information includes three figures and three tables and can be found with this article online at http://dx.doi.org/10.1016/j.stemcr.2014.03.007.

ACKNOWLEDGMENTS

We are grateful to Prof. F. Urano (Washington University School of Medicine) for valuable comments and analysis of ER stress, Prof. M. Amagai (Keio University) for skin biopsies, I. Kuki (Osaka City General Hospital) for providing patient medical information, T. Nagai (Keio University) for assistance with the TEM analyses, N. Kuzumaki (Keio University) for technical assistance, and all of the members of H.O.'s laboratory for their encouragement and support. This work was supported by funding from the Project for the Realization of Regenerative Medicine and Support for Core Institutes for iPS Cell Research from the Ministry of Education, Culture; Support for the Core Institutes for iPS Cell Research from the Ministry of Education, Culture, Sports, Science and Technology of Japan (MEXT; to H.O.); and a Grant-in-Aid for the Global COE Program from MEXT to Keio University. This work was also supported by a Grant-in-Aid for Young Scientists (B) from MEXT, a Keio University Grant-in-Aid for the Encouragement of Young Medical Scientists to Y.K.-N. from the Kanrinmaru-Project at Keio University, a Grant-in-Aid for Young Scientists (A) and a Grant-in-Aid for Scientific Research on Innovative Areas (Comprehensive Brain Science Network) from MEXT, and JST-CIRM Collaborative Research Program funding awarded to Y.O. H.O. is a scientific consultant for SanBio, Inc., Eisai, Co., Ltd., and Daiichi Sankyo, Co., Ltd. M.S. and A.N. are employed by Takeda Pharmaceutical Company Limited. S.Y. is a member without salary of the scientific advisory boards of iPierian, iPS Academia Japan, Megakaryon Corporation, and HEALIOS K. K. Japan.

Received: October 8, 2013
Revised: March 20, 2014
Accepted: March 20, 2014
Published: April 24, 2014

REFERENCES

Fan, J., Long, H., Li, Y., Liu, Y., Zhou, W., Li, Q., Yin, G., Zhang, N., and Cai, W. (2013). Edaravone protects against glutamate-induced PERK/EIF2α/ATF4 integrated stress response and activation of caspase-12. Brain Res. *1519*, 1–8.

Gencic, S., Abuelo, D., Ambler, M., and Hudson, L.D. (1989). Pelizaeus-Merzbacher disease: an X-linked neurologic disorder of myelin metabolism with a novel mutation in the gene encoding proteolipid protein. Am. J. Hum. Genet. *45*, 435–442.

Gow, A., and Lazzarini, R.A. (1996). A cellular mechanism governing the severity of Pelizaeus-Merzbacher disease. Nat. Genet. *13*, 422–428.

Gow, A., Friedrich, V.L., Jr., and Lazzarini, R.A. (1994). Many naturally occurring mutations of myelin proteolipid protein impair its intracellular transport. J. Neurosci. Res. *37*, 574–583.

Gow, A., Gragerov, A., Gard, A., Colman, D.R., and Lazzarini, R.A. (1997). Conservation of topology, but not conformation, of the proteolipid proteins of the myelin sheath. J. Neurosci. *17*, 181–189.

Gow, A., Southwood, C.M., and Lazzarini, R.A. (1998). Disrupted proteolipid protein trafficking results in oligodendrocyte apoptosis in an animal model of Pelizaeus-Merzbacher disease. J. Cell Biol. *140*, 925–934.

Griffiths, I., Klugmann, M., Anderson, T., Yool, D., Thomson, C., Schwab, M.H., Schneider, A., Zimmermann, F., McCulloch, M., Nadon, N., and Nave, K.A. (1998). Axonal swellings and degeneration in mice lacking the major proteolipid of myelin. Science *280*, 1610–1613.

Hodes, M.E., Aydanian, A., Dlouhy, S.R., Whelan, D.T., Heshka, T., and Ronen, G. (1998). A de novo mutation (C755T; Ser252Phe) in exon 6 of the proteolipid protein gene responsible for Pelizaeus-Merzbacher disease. Clin. Genet. *54*, 248–249.

Hu, B.Y., Du, Z.W., and Zhang, S.C. (2009). Differentiation of human oligodendrocytes from pluripotent stem cells. Nat. Protoc. *4*, 1614–1622.

Imaizumi, Y., Okada, Y., Akamatsu, W., Koike, M., Kuzumaki, N., Hayakawa, H., Nihira, T., Kobayashi, T., Ohyama, M., Sato, S., et al. (2012). Mitochondrial dysfunction associated with increased oxidative stress and α-synuclein accumulation in PARK2 iPSC-derived neurons and postmortem brain tissue. Mol. Brain *5*, 35.

Izrael, M., Zhang, P., Kaufman, R., Shinder, V., Ella, R., Amit, M., Itskovitz-Eldor, J., Chebath, J., and Revel, M. (2007). Human oligodendrocytes derived from embryonic stem cells: Effect of noggin on phenotypic differentiation in vitro and on myelination in vivo. Mol. Cell. Neurosci. *34*, 310–323.

Kang, S.M., Cho, M.S., Seo, H., Yoon, C.J., Oh, S.K., Choi, Y.M., and Kim, D.W. (2007). Efficient induction of oligodendrocytes from human embryonic stem cells. Stem Cells *25*, 419–424.

Lim, M.P., Devi, L.A., and Rozenfeld, R. (2011). Cannabidiol causes activated hepatic stellate cell death through a mechanism of endoplasmic reticulum stress-induced apoptosis. Cell Death Dis. *2*, e170.

Mikoshiba, K., Okano, H., Tamura, T., and Ikenaka, K. (1991). Structure and function of myelin protein genes. Annu. Rev. Neurosci. *14*, 201–217.

Nori, S., Okada, Y., Yasuda, A., Tsuji, O., Takahashi, Y., Kobayashi, Y., Fujiyoshi, K., Koike, M., Uchiyama, Y., Ikeda, E., et al. (2011). Grafted human-induced pluripotent stem-cell-derived neurospheres promote motor functional recovery after spinal cord injury in mice. Proc. Natl. Acad. Sci. USA *108*, 16825–16830.

Ohta, S., Imaizumi, Y., Okada, Y., Akamatsu, W., Kuwahara, R., Ohyama, M., Amagai, M., Matsuzaki, Y., Yamanaka, S., Okano, H., and Kawakami, Y. (2011). Generation of human melanocytes from induced pluripotent stem cells. PLoS ONE *6*, e16182.

Okada, Y., Shimazaki, T., Sobue, G., and Okano, H. (2004). Retinoic-acid-concentration-dependent acquisition of neural cell identity during in vitro differentiation of mouse embryonic stem cells. Dev. Biol. *275*, 124–142.

Okada, Y., Matsumoto, A., Shimazaki, T., Enoki, R., Koizumi, A., Ishii, S., Itoyama, Y., Sobue, G., and Okano, H. (2008). Spatiotemporal recapitulation of central nervous system development by murine embryonic stem cell-derived neural stem/progenitor cells. Stem Cells *26*, 3086–3098.

Seitelberger, F. (1995). Neuropathology and genetics of Pelizaeus-Merzbacher disease. Brain Pathol. *5*, 267–273.

Shimada, H., Okada, Y., Ibata, K., Ebise, H., Ota, S., Tomioka, I., Nomura, T., Maeda, T., Kohda, K., Yuzaki, M., et al. (2012). Efficient derivation of multipotent neural stem/progenitor cells from non-human primate embryonic stem cells. PLoS ONE *7*, e49469.

Shimojima, K., Inoue, T., Imai, Y., Arai, Y., Komoike, Y., Sugawara, M., Fujita, T., Ideguchi, H., Yasumoto, S., Kanno, H., et al. (2012). Reduced PLP1 expression in induced pluripotent stem cells derived from a Pelizaeus-Merzbacher disease patient with a partial PLP1 duplication. J. Hum. Genet. *57*, 580–586.

Southwood, C.M., Garbern, J., Jiang, W., and Gow, A. (2002). The unfolded protein response modulates disease severity in Pelizaeus-Merzbacher disease. Neuron *36*, 585–596.

Takahashi, K., Tanabe, K., Ohnuki, M., Narita, M., Ichisaka, T., Tomoda, K., and Yamanaka, S. (2007). Induction of pluripotent stem cells from adult human fibroblasts by defined factors. Cell *131*, 861–872.

Thomson, C.E., Montague, P., Jung, M., Nave, K.A., and Griffiths, I.R. (1997). Phenotypic severity of murine Plp mutants reflects in vivo and in vitro variations in transport of PLP isoproteins. Glia *20*, 322–332.

Wang, S., Bates, J., Li, X., Schanz, S., Chandler-Militello, D., Levine, C., Maherali, N., Studer, L., Hochedlinger, K., Windrem, M., and Goldman, S.A. (2013). Human iPSC-derived oligodendrocyte progenitor cells can myelinate and rescue a mouse model of congenital hypomyelination. Cell Stem Cell *12*, 252–264.

Yin, X., Baek, R.C., Kirschner, D.A., Peterson, A., Fujii, Y., Nave, K.A., Macklin, W.B., and Trapp, B.D. (2006). Evolution of a neuroprotective function of central nervous system myelin. J. Cell Biol. *172*, 469–478.

Expanding the phenotypic spectrum of *TUBB4A*-associated hypomyelinating leukoencephalopathies

Satoko Miyatake, MD, PhD
Hitoshi Osaka, MD, PhD
Masaaki Shiina, MD, PhD
Masayuki Sasaki, MD, PhD
Jun-ichi Takanashi, MD, PhD
Kazuhiro Haginoya, MD, PhD
Takahito Wada, MD, PhD
Masafumi Morimoto, MD, PhD
Naoki Ando, MD, PhD
Yoji Ikuta, MD
Mitsuko Nakashima, MD, PhD
Yoshinori Tsurusaki, PhD
Noriko Miyake, MD, PhD
Kazuhiro Ogata, MD, PhD
Naomichi Matsumoto, MD, PhD
Hirotomo Saitsu, MD, PhD

Correspondence to Dr. Matsumoto: naomat@yokohama-cu.ac.jp or Dr. Saitsu: hsaitsu@yokohama-cu.ac.jp

Supplemental data at Neurology.org

ABSTRACT

Objective: We performed whole-exome sequencing analysis of patients with genetically unsolved hypomyelinating leukoencephalopathies, identifying 8 patients with *TUBB4A* mutations and allowing the phenotypic spectrum of *TUBB4A* mutations to be investigated.

Methods: Fourteen patients with hypomyelinating leukoencephalopathies, 7 clinically diagnosed with hypomyelination with atrophy of the basal ganglia and cerebellum (H-ABC), and 7 with unclassified hypomyelinating leukoencephalopathy, were analyzed by whole-exome sequencing. The effect of the mutations on microtubule assembly was examined by mapping altered amino acids onto 3-dimensional models of the αβ-tubulin heterodimer.

Results: Six heterozygous missense mutations in *TUBB4A*, 5 of which are novel, were identified in 8 patients (6/7 patients with H-ABC [the remaining patient is an atypical case] and 2/7 patients with unclassified hypomyelinating leukoencephalopathy). In 4 cases with parental samples available, the mutations occurred de novo. Analysis of 3-dimensional models revealed that the p.Glu410Lys mutation, identified in patients with unclassified hypomyelinating leukoencephalopathy, directly impairs motor protein and/or microtubule-associated protein interactions with microtubules, whereas the other mutations affect longitudinal interactions for maintaining αβ-tubulin structure, suggesting different mechanisms in tubulin function impairment. In patients with the p.Glu410Lys mutation, basal ganglia atrophy was unobserved or minimal although extrapyramidal features were detected, suggesting its functional impairment.

Conclusions: *TUBB4A* mutations cause typical H-ABC. Furthermore, *TUBB4A* mutations associate cases of unclassified hypomyelinating leukoencephalopathies with morphologically retained but functionally impaired basal ganglia, suggesting that *TUBB4A*-related hypomyelinating leukoencephalopathies encompass a broader clinical spectrum than previously expected. Extrapyramidal findings may be a key for consideration of *TUBB4A* mutations in hypomyelinating leukoencephalopathies. ***Neurology*®** 2014;82:2230–2237

GLOSSARY

4H = hypomyelination, hypodontia, and hypogonadotropic hypogonadism; **H-ABC** = hypomyelination with atrophy of the basal ganglia and cerebellum; **MAP** = microtubule-associated protein; **MREI** = Met-Arg-Glu-Ile; ***TUBB4A*** = tubulin, beta 4A class IVa.

Leukoencephalopathies are a heterogeneous group of disorders affecting the white matter of the brain. It is estimated that approximately 30% to 40% of patients with leukoencephalopathy remain without a specific diagnosis despite extensive investigations.[1] Brain MRI aids diagnosis because distinct MRI patterns enable easier detection of white matter abnormalities and successful categorization.[1,2] Moreover, recent advances in whole-exome sequencing have improved understanding of these clinically defined/undefined disease entities by identifying genetic causes and their phenotypic spectrum. For example, the majority of cases with hypomyelination,

From the Departments of Human Genetics (S.M., M.N., Y.T., N. Miyake, N. Matsumoto, H.S.) and Biochemistry (M. Shiina, K.O.), Yokohama City University Graduate School of Medicine; Division of Neurology (H.O.), Clinical Research Institute, Kanagawa Children's Medical Center, Yokohama; Department of Pediatrics (H.O.), Jichi Medical School, Tochigi; Department of Child Neurology (M. Sasaki), National Center of Neurology and Psychiatry, Tokyo; Department of Pediatrics (J.-i.T.), Kameda Medical Center, Chiba; Department of Pediatric Neurology (K.H.), Takuto Rehabilitation Center for Children, Sendai; Genetic Counselling and Clinical Research Unit (T.W.), Kyoto University School of Public Health; Department of Pediatrics (M.M.), Graduate School of Medical Science, Kyoto Prefectural University of Medicine; Department of Neonatology and Pediatrics (N.A.), Nagoya City University Graduate School of Medical Sciences; and Department of Neurology (Y.I.), Tokyo Metropolitan Children's Medical Center, Japan.

Go to Neurology.org for full disclosures. Funding information and disclosures deemed relevant by the authors, if any, are provided at the end of the article.

hypodontia, and hypogonadotropic hypogonadism (4H syndrome),[3–5] tremor-ataxia with central hypomyelination leukodystrophy (TACH),[6] leukodystrophy with oligodontia (LO),[7,8] or hypomyelination with cerebellar atrophy and hypoplasia of the corpus callosum (HCAHC),[9] which was described in Japan, share some clinical overlap and have *POLR3A* or *POLR3B* mutations in common.[10–14]

Hypomyelination with atrophy of the basal ganglia and cerebellum (H-ABC)[15,16] is characterized by early-onset motor regression and/or delay followed by extrapyramidal symptoms, distinguishing H-ABC from other hypomyelinating leukoencephalopathies caused by *POLR3A* or *POLR3B* mutations. A recurrent de novo *TUBB4A* mutation was recently reported in 11 patients with H-ABC.[17] Of note, *TUBB4A* mutations also cause autosomal dominant DYT4 dystonia,[18,19] a condition that presents with normal brain MRI findings. This suggests that in addition to H-ABC, *TUBB4A* mutations may be widely related to other hypomyelinating leukoencephalopathies. Herein, we describe 8 patients with *TUBB4A* mutations identified by whole-exome sequencing, clarifying their phenotypic spectrum.

METHODS Study subjects. Fourteen patients with molecularly undiagnosed hypomyelinating leukoencephalopathy were included in the study. Patients were diagnosed based on clinical symptoms and brain MRI findings. Among the 14 patients, 7 were clinically diagnosed with H-ABC and 7 with hypomyelinating leukoencephalopathy that did not meet the criteria for H-ABC, 4H syndrome, or Pelizaeus-Merzbacher disease. Patients with *POLR3A* or *POLR3B* mutations were excluded from this cohort. When available, parental samples were also tested in mutation-positive patients.

Standard protocol approvals, registrations, and patient consents. Experimental protocols were approved by the Committee for Ethical Issues at Yokohama City University School of Medicine. Written informed consent was obtained from all patients or their parents.

Mutation analysis. We performed whole-exome sequencing in 14 patients. Genomic DNA was captured using the SureSelect^{XT} Human All Exon 50 Mb (v3) or 51 Mb (v4) Kit (Agilent Technologies, Santa Clara, CA) and sequenced on either the GAIIx platform (Illumina, San Diego, CA) with 108–base pair paired-end reads or HiSeq2000 (Illumina) with 101–base pair paired-end reads. After filtering against dbSNP135 and 91 in-house normal control exomes, rare protein-altering and splice-site variant calls were obtained for each patient. We identified *TUBB4A* mutation calls and confirmed these mutations by Sanger sequencing. In 4 of 8 patients with *TUBB4A* mutations, parental samples were analyzed by Sanger sequencing to determine the mode of inheritance.

Three-dimensional structure modeling. To determine the effect of *TUBB4A* mutations on microtubule assembly, we mapped mutation positions onto the 3-dimensional structure of the αβ-tubulin heterodimer (Protein Data Bank code 1JFF)[20] and examined their interaction with surrounding molecules.

RESULTS Identification of *TUBB4A* mutations. Whole-exome sequencing identified 6 heterozygous missense mutations in *TUBB4A*, in 6 of 7 patients with H-ABC (85.7%) and 2 of 7 patients with unclassified hypomyelinating leukoencephalopathy (28.6%) (see table 1 and tables e-1 and e-2 on the *Neurology*® Web site at Neurology.org). Two mutations, c.1228G>A (p.Glu410Lys) and c.745G>A (p.Asp249Asn), were identified in 2 unrelated patients. Two hypomyelinating patients with similar clinical features as those previously reported,[9] carried the c.1228G>A mutation. The c.745G>A mutation was a recurrent mutation reported in patients with H-ABC.[17] The other 5 mutations were novel. None of the mutations were registered in the National Heart, Lung, and Blood Institute Exome Sequencing Project (ESP6500), 1000 Genomes, or our 575 in-house control exomes. The c.5G>A (p.Arg2Gln) missense mutation, identified in a patient with H-ABC, alters Arg2 to Gln. Arg2 is located within the highly conserved, amino-terminal β-tubulin tetrapeptide Met-Arg-Glu-Ile (MREI) motif and is involved in autoregulatory mechanisms for β-tubulin stability. Notably, Arg2 is altered to Gly in a large family with DYT4.[18,19] All of the mutations occur within highly conserved residues, from yeast to human, and among human β-tubulins (figure 1). GERP (Genomic Evolutionary Rate Profiling) scores were high for all mutated residues, and Web-based prediction programs identified all mutations as pathogenic (table e-1). In 4 patients with parental samples available, the mutations occurred de novo (table e-1). In 2 patients, only the mother's sample was available and confirmed as mutation-negative.

Three-dimensional structural modeling analysis. Tubulin heterodimers polymerize longitudinally in a head-to-tail manner, forming protofilaments, which then laterally interact with each other to form microtubules (figure 2). Some mutations fall within longitudinal interaction interfaces, whereas others are near interaction regions for motor proteins and microtubule-associated proteins (MAPs).[21,22] Thr178 of β-tubulin is located at a longitudinal interheterodimer interface, in proximity to the guanine nucleotide–binding pocket of β-tubulin (figure 2). This residue is reportedly important for regulation of αβ-tubulin heterodimer polymerization with GTP[23,24]; therefore, the Thr178Arg mutation may affect the polymerization process. Arg2 and Asp249 of β-tubulin are

Table 1 Clinical features of the patients

	Patient 1[9]	Patient 2[9]	Patient 3	Patient 4[26]	Patient 5[27]	Patient 6	Patient 7	Patient 8
Current age, y, sex	23, M	41, M	15, F	12, M	16, M	10, M	4, M	1, F
Mutation	c.1228G>A	c.1228G>A	c.5G>A	c.745G>A	c.1162A>G	c.745G>A	c.533C>G	c.785G>A
Protein alteration	p.Glu410Lys	p.Glu410Lys	p.Arg2Gln	p.Asp249Asn	p.Met388Val	p.Asp249Asn	p.Thr178Arg	p.Arg262His
Initial diagnosis	Unclassified hypomyelinating leukoencephalopathy[a]	Unclassified hypomyelinating leukoencephalopathy[a]	H-ABC	H-ABC	H-ABC	H-ABC	H-ABC	H-ABC
Age at onset, mo	12	12	1.5	18	3	19	6	2
Maximum motor milestone	Unsupported unstable walking	Unsupported unstable walking	No head control	Walking for a few steps	Rolling over	Supported walking	No head control	No head control
Onset of motor deterioration	10 y	20 y	ND	18 mo	3 mo	19 mo	ND	ND
Intellectual disability	Mild	Moderate	Severe	Severe	Severe	Severe	Severe	Moderate
Motor signs								
Ataxia	+	+	ND	+	ND	+	ND	ND
Tremor	+	+	–	–	–	+	–	ND
Spasticity	+	+	+	+	+	+	ND	+
Babinski sign	+	+	–	+	ND	+	–	+
Rigidity	+	+	+	+	+	+	+	–
Choreoathetosis	–	–	+	+	+	–	–	–
Dystonia	+	+	+	+	+	+	–	–
Brain MRI findings								
Hypomyelination	+	+	+	+	+	+	+	+
Atrophy of the basal ganglia	–	±	+	+	+	+	+	+
Atrophy of the cerebellum	+	+	+	+	+	+	+	–
Atrophy of the corpus callosum	+	+	+	+	+	+	+	–

Abbreviations: H-ABC = hypomyelination with atrophy of the basal ganglia and cerebellum; ND = not determined.
Symbols: + = present; – = absent: ± = minimally detected.
[a] Unclassified hypomyelinating leukoencephalopathy: did not meet the criteria for H-ABC, 4H syndrome (hypomyelination, hypodontia, and hypogonadotropic hypogonadism), or Pelizaeus-Merzbacher disease.

located at an intraheterodimer interface (figures 2 and e-1A). These residues stabilize the β-tubulin T7 loop region, which interacts with α-tubulin within a heterodimer (figure e-1A), indicating that the p.Arg2Gln and p.Asp249Asn mutations may affect tubulin heterodimerization. Glu410 is located on the exposed outer surface that mediates interactions with motor proteins and/or MAPs (figures 2 and e-1B).[21,22] This residue is crucial for the kinesin-microtubule interaction, and thus the p.Glu410Lys mutation may directly impair motor protein and/or MAP interactions with microtubules. Arg262 and Met388 are located near the intra- and interheterodimer interfaces, respectively, and both are also near the interaction region for motor proteins and/or MAPs (figures 2 and e-1, B and C). Arg262 is involved in the hydrophobic core with residues from a loop that interacts with the α-tubulin subunit within the heterodimer, and from helix H12, which interacts with motor proteins and/or MAPs (figures 2 and e-1B). Met388 is involved in the hydrophobic core with residues from helix H11, which interacts with the α-tubulin subunit in the neighboring heterodimer, and from helix H12 (figures 2 and e-1C).[25] Thus, the p.Arg262His and the p.Met388Val mutations may destabilize the hydrophobic core and potentially affect the tertiary structure, resulting in impairment of longitudinal intra- and interheterodimer tubulin interactions, respectively, and/or interaction with motor proteins and/or MAPs.

Clinical features. Clinical information on patients with *TUBB4A* mutations is presented in tables 1 and e-2, and brain MRIs are shown in figures 3 and e-2.

The mean age at onset was 9.2 months, although the age at onset was varied. Initial motor development also varied, with some acquiring unsupported but

Figure 1 ***TUBB4A*** **mutations in patients with hypomyelinating leukoencephalopathy**

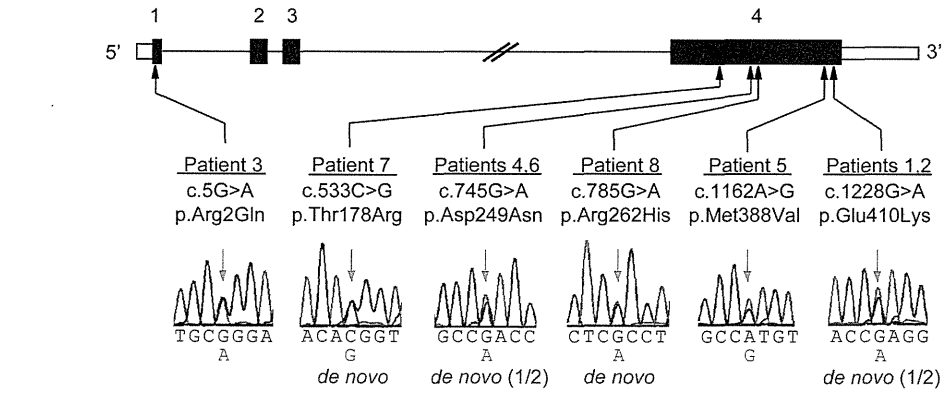

Amino acid change	Q	R	N	H	V	K
H. sapiens_TUBB4A	MREIVHL	VSDTVVE	LNADLRK	PFPRLHF	FTAMFRR	EFTEAES
M. musculus_TUBB4A	MREIVHL	VSDTVVE	LNADLRK	PFPRLHF	FTAMFRR	EFTEAES
B. Taurus_TUBB4A	MREIVHL	VSDTVVE	LNADLRK	PFPRLHF	FTAMFRR	EFTEAES
X. tropicalis_TUBB4A	MREIVHL	VSDTVVE	LNADLRK	PFPRLHF	FTAMFRR	EFTEAES
D. rerio_TUBB2C	MREIVHL	VSDTVVE	LNADLRK	PFPRLHF	FTAMFRR	EFTEAES
TUBB4B_Human	MREIVHL	VSDTVVE	LNADLRK	PFPRLHF	FTAMFRR	EFTEAES
TUBB2B_Human	MREIVHI	VSDTVVE	LNADLRK	PFPRLHF	FTAMFRR	EFTEAES
TBB1_Human	MREIVHI	VSDTVVE	LNADLRK	PFPRLHF	FSAMFRR	EFGEAES
TBB_YEAST	MREIVHI	TSDTVVE	LNADLRK	PFPRLHF	FSAMFRR	EFSEAES

TUBB4A schematic with the 6 mutations is presented. Untranslated regions and coding regions are shown in white and black rectangles, respectively. All mutations occur at evolutionarily conserved amino acids. Homologous sequences were aligned using CLUSTALW (http://www.genome.jp/tools/clustalw/).

unsteady walking and others never acquiring head control. The maximum motor milestone of these patients was unstable short walking. The clinical course appeared milder in patients with an older age at onset. This tendency was most prominent in patients initially diagnosed with unclassified hypomyelinating leukoencephalopathy. For example, the onset of motor deterioration started in the first or second decades in these patients but was between 0 and 3 years old in patients with typical H-ABC. Intellectual disability was mild to moderate in the former but mostly severe in the latter patients.

All clinically evaluated patients with *TUBB4A* mutations demonstrated cerebellar ataxia and spasticity. Except for patient 8, all demonstrated extrapyramidal features such as rigidity, dystonia, or choreoathetosis. In patient 1, dystonia was prominent compared with other hypomyelination patients with either *POLR3A* or *POLR3B* mutations.[9,11] Patient 8 was 1 year old at the time of the study, and brain MRI showed a relatively small but still well-retained putamen compared with healthy subjects of the same age, suggesting that extrapyramidal features may not yet have developed but would likely express as the basal ganglia atrophy progressed. Notably, both hypomyelinating patients with either very mild basal ganglia atrophy (patient 2) or none identifiable (patient 1) demonstrated extrapyramidal signs, suggesting that the basal ganglia may be impaired functionally in these patients as well as other patients with typical H-ABC. Case reports are available in appendix e-1. Patients 1 and 2,[9] 4,[26] and 5[27] were previously described. Retrospectively, patient 2 might be diagnosed with atypical H-ABC because minimal basal ganglia atrophy cannot be excluded. In the patient with H-ABC with no *TUBB4A* mutation, the atrophy of basal ganglia was very mild compared with that of patients with typical H-ABC. However, clinical symptoms are very severe with neither head control nor sitting at 12 years, suggesting that the patient has atypical H-ABC.

DISCUSSION The β- and α-tubulins are major components of microtubules. Microtubules have essential roles in many cellular processes including mitosis, intracellular transport, asymmetric neuronal morphology, and ciliary and flagellar motility.[28] Multiple β-tubulin isotypes are present, with high homology (differing primarily at 15–20 amino acids within the C terminus), and expressed differentially in a tissue-dependent manner.[29] Certain isotypes, namely, β-tubulin isotypes 2A, 2B, 3, and 4A, are neuron-specific proteins and highly expressed in brain.[28] In the nervous system, microtubules provide structure, generate force necessary for neuronal migration, and serve as scaffolds for motor proteins and/or MAPs to transport cargo.[30] In addition to *TUBB4A*-associated leukoencephalopathies[17] and dystonia,[18,19] *TUBA1A*, *TUBB2B*, and *TUBB3*

Figure 2 Structural prediction of *TUBB4A* mutations in the αβ-tubulin heterodimer

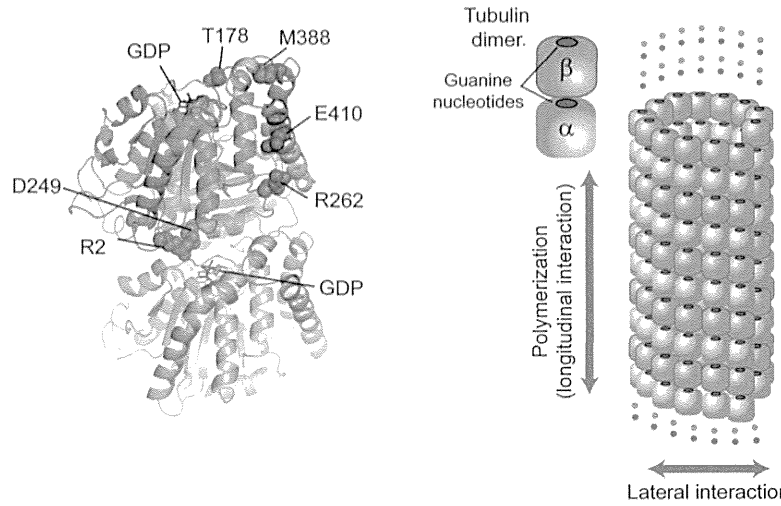

Mapping of disease-causing amino acid mutations on the αβ-tubulin heterodimer (Protein Data Bank code 1JFF) crystal structure, with schematic representation of a tubulin dimer (left) and microtubule segment (right). The α- and β-tubulins are colored gray and green, respectively. Left: The longitudinal interheterodimer interface of β-tubulin (which interacts with α-tubulin in a neighboring αβ heterodimer) is colored pink,[24] and the β-tubulin microtubule-associated protein and motor protein interaction region is colored cyan.[21,22] Side chains of residues altered by the mutations are shown in space-filling representation in red. Helices, β-sheets, and loops are shown as ribbons, arrows, and threads, respectively, and nucleotides are blue sticks. Right: Tubulin heterodimers polymerize longitudinally to form protofilaments (longitudinal interaction), then laterally interact with each other to form microtubules (lateral interaction). Blue circles represent guanine nucleotide–binding pockets of α- and β-tubulins.

mutations are reported to cause the spectrum of neurologic disorders resulting from neural migration, differentiation, and axon guidance and maintenance abnormalities,[25] demonstrating the importance of αβ-tubulin heterodimers in the nervous system.

In this study, we identified 6 missense *TUBB4A* mutations, 5 of which are novel, in 6 of 7 patients with H-ABC and 2 of 7 patients initially diagnosed with unclassified hypomyelinating leukoencephalopathy. Of the patients with H-ABC, all 6 patients with *TUBB4A* mutations showed typical H-ABC, supporting that H-ABC is a distinct disease entity caused by *TUBB4A* abnormality. We did not detect any *TUBB4A* mutations in one patient with atypical H-ABC. This may be because this patient has a clinically similar, but different disease, possibly caused by a different mutated gene.

We report a *TUBB4A* mutation in 2 patients with preserved basal ganglia. Their brain MRI findings are similar to patients with *POLR3A* or *POLR3B* mutations, rather than H-ABC. However, it is notable that both patients showed apparent extrapyramidal signs, to suggest functional impairment. Accompanying extrapyramidal features are extremely atypical in patients with either *POLR3A* or *POLR3B* mutations.[9,11] Furthermore, comparing these 2 patients with other typical H-ABC patients with *TUBB4A* mutations, patients with minimal basal ganglia atrophy tend to have a milder clinical course. Both patients have a recurrent missense mutation, c.1228G>A (p.Glu410Lys). Based on our 3-dimensional modeling analysis, the Glu410Lys mutation is predicted to directly impair motor protein and/or MAP interactions with microtubules, while the other mutations identified in patients with typical H-ABC may affect longitudinal interactions for maintaining αβ-tubulin heterodimerization/polymerization. Different effects of the *TUBB4A* mutations on tubulin function may lead to this phenotypic variation. Supporting this hypothesis, the p.Glu410Lys mutation in *TUBB3*, which also directly alters a kinesin motor protein binding site in β-tubulin isotype 3, demonstrates clinically distinct features compared with the other mutations.[30] Therefore, the p.Glu410Lys mutation in *TUBB4A* may contribute to the milder end of the phenotypic spectrum of *TUBB4A* mutations. Additional patients with *TUBB4A* mutations are needed to clinically confirm mutational consequences.

Another important finding is that one of the patients with H-ABC had a p.Arg2Gln mutation, since the p.Arg2Gly mutation has recently been identified in patients from a large DYT4 family.[18,19] DYT4 was described in 1985 in an Australian family that had emigrated from England as whispering dysphonia and generalized dystonia. To date, no other pedigrees